Title

Structure and inhibition mechanism of the helicase-primase complex from human herpesvirus 1

Author list

Ko Sato[1], Hisashi Ishida[2], Toma Miyagishi[3], Shunsuke Kobayashi[1], Yoshiaki Kise[4], Keisuke Hamada[1], Chikako Okada[1], Asako Oguni[1], Osamu Nureki[4], Hidetoshi Kono[2], Kaori Fukuzawa[3], Toru Sengoku[1,*]

Affiliations

[1]Department of Biochemistry, Yokohama City University Graduate School of Medicine, Kanagawa, Japan

[2]Insitute for Quantum Life Science, National Institutes for Quantum Science and Technology, Chiba, Japan

[3]Graduate School of Pharmaceutical Sciences, Osaka University, Osaka, Japan

[4]Department of Biological Sciences, Graduate School of Science, The University of Tokyo, Tokyo, Japan

*To whom correspondence should be addressed:

tsengoku@yokohama-cu.ac.jp

Abstract

Human herpesviruses (HHVs) are widespread pathogens that can cause severe disease, particularly in immunocompromised individuals, and have been increasingly associated with chronic conditions such as Alzheimer's disease and multiple sclerosis. Most antiviral therapies target the α-subfamily of HHVs, while treatment options for the β- and γ-subfamilies remain limited. A key antiviral target in α-subfamily is the helicase-primase complex (HPC), which is essential for viral DNA replication; however, its structure and inhibition mechanism have remained unclear. Here, we report the cryo-EM structures of the HPC from human herpesvirus 1 (HHV1) bound to single-stranded DNA(ssDNA) and either of two clinical inhibitors, amenamevir or pritelivir. The HPC comprises flexible helicase and primase modules, and both inhibitors engage a shared allosteric pocket near the ATPase site. Structural, biochemical, and molecular dynamics analyses reveal that these inhibitors lock the helicase in an open, inactive conformation, thereby preventing ATP binding and DNA unwinding. Furthermore, quantitative interaction energy analysis by fragment molecular orbital (FMO) calculation elucidates why these inhibitors are α-subfamily selective and how subtle chemical differences between amenamevir and pritelivir lead to distinct antiviral spectra. Our findings clarify the inhibition mechanism of clinically relevant HPC inhibitors and provide a structural basis for their subfamily selectivity. This framework may guide the rational design of next-generation inhibitors with altered herpesvirus specificity and provide broader insights into the development of helicase-targeted therapeutics.

42 **Introduction**

43 Human Herpesviruses (HHVs) are significant human pathogens[1]. To date, eight
44 herpesviruses (HHV1–8) have been identified and classified into three subfamilies: α, β,
45 and γ. All these herpesviruses can cause human diseases, including herpes simplex, herpes
46 zoster, encephalitis, and various tumors. They can also lead to severe conditions,
47 particularly in immunocompromised individuals. Moreover, recent studies have suggested
48 potential links between herpesvirus infections and chronic diseases such as Alzheimer's
49 disease[2], dementia[3], multiple sclerosis[4], and chronic fatigue syndrome[5]. Currently, multiple
50 anti-herpes drugs, such as nucleoside analogs and helicase-primase inhibitors (HPIs), are
51 available for the α-subfamily (HHV1/HSV1, HHV2/HSV2, and HHV3/VZV). In contrast,
52 therapeutic options for the β-subfamily (HHV4/Epstein-Barr virus and HHV8/Kaposi's
53 sarcoma-associated virus) and γ-subfamily (HHV5/cytomegalovirus, HHV6, and HHV7)
54 remain limited, underscoring the need to develop new antiviral drugs targeting these
55 subfamilies.

56 Herpesviruses employ a set of unique enzymes for the replication of their genomes, which
57 can be therapeutically targeted by specific inhibitors. One such target is the helicase-
58 primase complex (HPC)[6], composed of three subunits: the helicase subunit (UL5 in
59 HHV1), the primase subunit (UL52 in HHV1), and a non-catalytic accessory subunit (UL8
60 in HHV1). The HPC associates with the replication fork and unwinds the DNA duplex
61 through the action of the helicase subunit, generating ssDNA as the templates for DNA
62 synthesis by the viral DNA polymerase. While most replicative helicases in eukaryotes and

63 prokaryotes form hexameric ring structures surrounding the DNA[7], herpesvirus helicases
64 belong to superfamily Ib, which is thought to function as monomers[8]. Previous studies on
65 related superfamily Ib helicases have shown that they alternate between "open" and
66 "closed" conformations in an ATP hydrolysis-dependent manner, translocating along
67 ssDNA in an inchworm-like motion to separate the base pairs they encounter[9]. The HPC
68 also synthesizes an RNA primer on the lagging strand through the action of the primase
69 subunit. This subunit contains sequence motifs conserved among archaeo-eukaryotic
70 primases[10], along with a putative zinc-binding domain (ZBD), which is commonly found in
71 other primases, including the human PrimPol protein. Notably, all three subunits of the
72 HPC are required for the optimal activities of both the helicase and primase, suggesting
73 complex regulatory interactions between them. As no experimental structure of the HPC
74 has been determined, it remains elusive how these subunits interact with each other, how
75 the two catalytic domains are spatially arranged, and how the two activities are coordinated
76 within this unique complex.

77 HPIs specifically inhibit the HPC of α-subfamily, thereby suppressing their replication. One
78 such molecule, amenamevir (AMNV)[11,12] has demonstrated efficacy against all three α-
79 herpesviruses, HHV1 and 2 (also known as herpes simplex viruses 1 and 2, respectively),
80 and HHV3 (varicella zoster virus). AMNV has been approved in Japan for the treatment of
81 herpes simplex and herpes zoster; however, its poor brain penetration[13] limits its clinical
82 utility for treating herpesvirus-induced encephalitis. Pritelivir (PTV)[14,15], another clinical
83 HPI in phase 3, is effective against HHV1 and HHV2, but shows only limited activity

84 against HHV3 and HHV5[14]. To date, no HPIs effective against β- and γ-subfamily
85 herpesviruses have been reported.

86

87 **Main**

88 **Overall structure**

89 To elucidate the overall architecture of the HPC and the inhibition mechanism by HPIs, we
90 set out to determine its cryo-EM structures. We reconstituted the HPC of HHV1 by co-
91 expressing the three subunits in insect cells and purified the complex by affinity
92 chromatography. We mixed the purified HPC with a 43-mer ssDNA, AMP-PNP (a
93 nonhydrolyzable analog of ATP) and either AMNV or PTV, and collected cryo-EM images.
94 During the EM volume reconstruction, we noticed that the HPC can be divided into two
95 modules, hereafter referred to as the helicase module (HM) and the primase module (PM),
96 whose relative positions are flexible. Thus, following the global density reconstruction,
97 focused refinement of the two modules were independently performed, yielding two locally
98 refined maps with improved resolution (about 2.9-3.3 Å), on which we built atomic models
99 (Extended Data Figures 1-5). We also performed a 3DFlex refinement[16] of the overall
100 complex which gave a better overall resolution (about 3.1-3.3 Å) and built the full atomic
101 models into these 3DFlex maps with the help of the two atomic models built on locally
102 refined maps (Supplementary Movie 1). Unless otherwise stated, we use locally built
103 models to describe local interactions and the 3DFlex-derived models for discussion on
104 global structures.

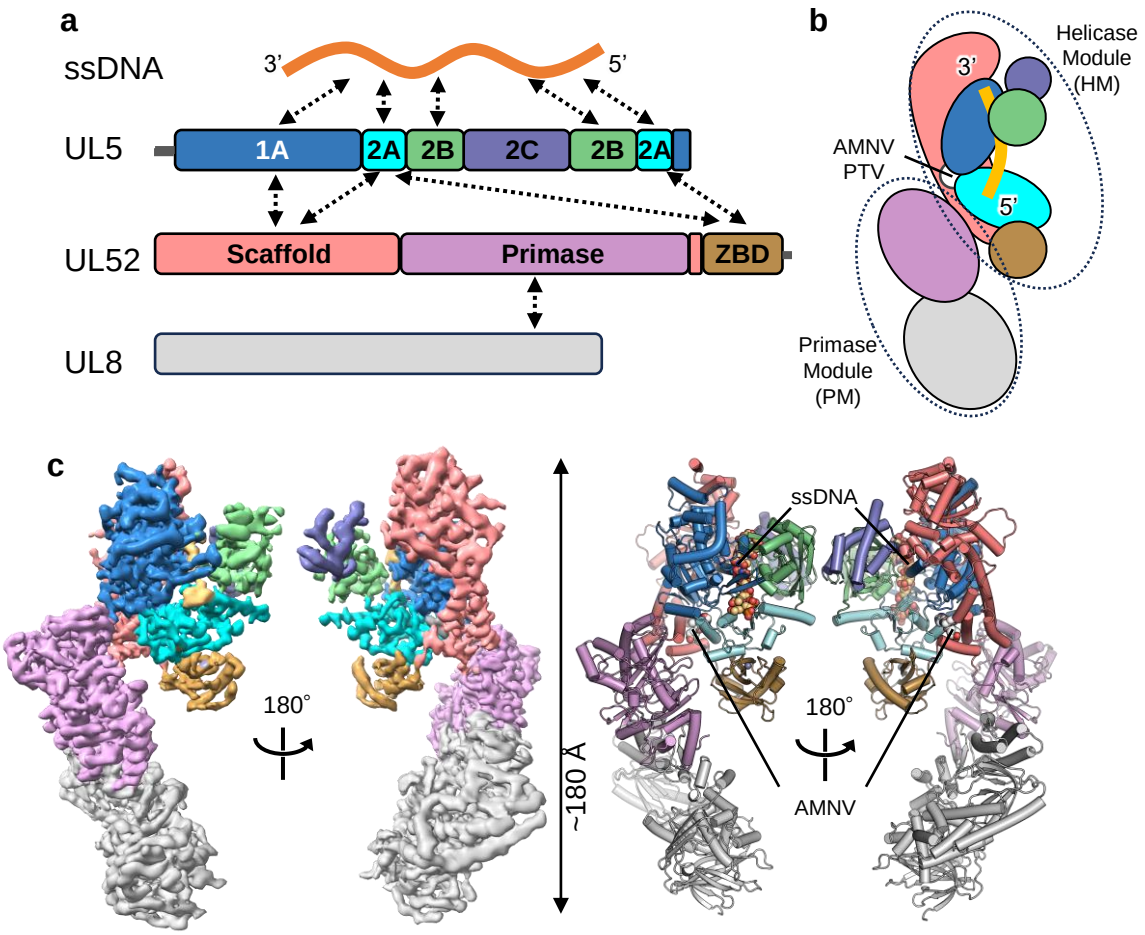

Figure 1: Overall structure of the AMNV-bound HPC from HHV1. a, Domain architectures of the three subunits and their interactions with each other and with ssDNA. The color scheme used in this panel is applied consistently throughout the paper to distinguish different domains. **b**, A cartoon illustration of the HPC. **c**, 3DFlex map (calculated using 3DFlex) and the ribbon model of the AMNV-bound HPC.

105 Figure 1 and Extended Data Figure 6 show the overall structures of the AMNV- and PTV-
106 bound complexes, respectively. The HM consists of the entire UL5 protein and two
107 domains of UL52, namely the scaffold domain (SD, residues 1-408 and 891-910) and the
108 ZBD (residues 911-1043). The two domains of UL52 intimately interact with UL5 with
109 large interface areas. UL5 consists of the domains 1A (residues 34-344 and 864-892), 2A
110 (residues 345-417 and 805-863), 2B (residues 418-514 and 693-804), and 2C (residues
111 515-692), which are shared by superfamily Ib helicases. Structure similarity analysis using
112 the DALI server[17] revealed that the helicase subunit is most similar to Pif1 helicases (e.g.,
113 PDB ID: 7OTJ; Z score = 19.2)[18–21]. Of the 43-mer ssDNA used for structural
114 determination, only seven nucleotides were clearly visible, bound to domains 1A, 2A, and
115 2B of UL5, with the 5′ and 3′ ends bound to domains 2A and 1A, respectively, in agreement
116 with other superfamily I and II helicases[8]. We tentatively modeled them as oligo-dT.
117 Notably, no density of AMP-PNP was observed at the ATPase active site of UL5 (discussed
118 later). The PM consists of the primase domain of UL52 (PD, residues 409-890) and the
119 entire UL8 protein, which interact with each other. The intimate interaction between UL5-
120 UL52 and UL52-UL8 explains why a lack of one subunit seriously affects the helicase and
121 primase activities of the remaining subunits.

122 AMNV and PTV bind to a shared pocket located near, but not at, the ATP-binding site. The
123 pocket is formed by the SD of UL52 and the linker region connecting domains 1A and 2A
124 of UL5 (designated as motif IIIa in superfamily I, although sometimes referred to as motif
125 IV)[8]. In the structures of superfamily Ia and Ib helicases[9,20,22], a conserved arginine residue
126 of motif IIIa (corresponding to R345 of UL5) directly interacts with the γ-phosphate group

127 of the bound ATP analogs. This suggests that motif IIIa plays a role in coupling ATP
128 binding/hydrolysis to domain movement—a process potentially influenced by binding of
129 HPIs. The two inhibitor-bound structures are nearly identical (the RMSD value of 0.50 Å
130 for 1,098 Cα atoms of the HM; Extended Data Figure 6), suggesting that the two inhibitors
131 likely function in essentially the same manner.

132 **PD and ZBD of UL52**

133 The DALI server search revealed that the PD is structurally similar to other archaeo-
134 eukaryotic primases, including human and bacterial PrimPol (e.g., PDB ID: 5L2X; Z-score
135 = 14.8) as well as viral helicase-primase fusion proteins (e.g., PDB ID: 8XJ6; Z-score =
136 12.7) whose helicase domains assemble into a hexameric ring. When a template DNA-
137 bound structure of PrimPol[23] is superposed, the superposed DNA is positioned with its 3'
138 end directed towards the HM, while the HM-bound ssDNA in the current HPC structure is
139 oriented with its 5' end toward the PM (Extended Data Figure 7a-c). This configuration is
140 consistent with a model in which a single HPC molecule engages the continuous template
141 strand via its HM and PM simultaneously. However, to accommodate a single ssDNA
142 spanning the two modules in a smooth conformation, substantial reorientation between
143 these two modules would be necessary. Given the apparent flexibility between the two
144 modules and the lack of a large interaction surface between them, it is possible such
145 reorientation occurs during the productive primer synthesis by the PD coupled with
146 replication fork progression driven by the HM. The HPC may engage the template DNA

147 through an alternative mechanism (e.g., two HPC molecules binding to a single replication
148 fork), as suggested earlier[24].

149 The ZBD coordinates a zinc ion via C988, H993, C1023, and C1028. The UL52 ZBD is
150 widely conserved among eukaryotic PrimPol proteins. Structural prediction using
151 AlphaFold2[25] revealed a strong similarity between the ZBD of UL52 and that of human
152 PrimPol (Extended Data Figure 7d, e). The human PrimPol ZBD possesses ssDNA-binding
153 activity and is required for primase activity. It has been proposed to bind template ssDNA
154 to regulate the primase and polymerase activities of PrimPol[26]. The reorientation of the HM
155 and PM domains may bring the PD and ZBD closer together, enabling such a cooperative
156 binding mode.

157 **UL8-PD interactions**

158 As predicted by a previous bioinformatic analysis[27], UL8 adopts a fold that is structurally
159 related to B-family DNA polymerases. However, UL8 lacks both the catalytic residues
160 required for coordinating divalent ions and the basic surface necessary for template DNA
161 binding (Extended Data Figure 8), consistent with its lack of detectable enzymatic activity.
162 At the UL52–UL8 interface, a network of salt bridges and hydrogen bonds is formed,
163 involving the R640 side chain and L748main chain of UL8, and the side chains of E511 and
164 R437 of UL52 (Extended Data Figure 8c). Notably, R640 is one of five residues that are
165 completely conserved among the eight human herpesviruses and was previously predicted
166 to be involved in UL52 binding based on a mutagenesis study[28].

167 **Helicase module and ssDNA binding**

168 The bound ssDNA interacts with the domains 1A, 2A, and 2B of UL5. Domains 1A and 2A
169 engage the DNA backbone mainly through hydrophilic interactions with the phosphate
170 groups, while domain 2B mostly forms van der Waals contacts with it (Figure 2a-e).
171 Nucleotides dT3-dT5 are wrapped around by the three domains and completely buried
172 within a channel that is too small to accommodate the double-stranded DNA (Figure 2a),
173 suggesting that like other superfamily I helicases, UL5 unwinds the DNA duplex via a
174 steric exclusion mechanism coupled with the translocation along the tracking strand.
175 Domain 2A binds the phosphate groups of dT2-dT4 via the conserved helicase motifs IV
176 and V, whereas domain 1A binds those of dT5-dT7 via motifs Ia and Ic. This binding mode
177 resembles those observed in other superfamily Ib helicases such as RecD2 and Pif1[9,18–20].
178 Substitution of T809 (motif V) with isoleucine was shown to impair viral DNA replication
179 and reduce both ATPase and helicase activities of the UL5-UL52 subcomplex[29,30].

180 The bound DNA is slightly curved, and base-stacking interactions are interrupted between
181 dT2 and dT3 and between dT5 and dT6 (Figure 2b-e). Two structural elements, the motif Ic
182 helix (residues 153-156) in domain 1A and a β-hairpin (residues 298-313, unique to UL5)
183 of domain 2A, are inserted between the neighboring bases at these positions, respectively,
184 likely stabilizing the curved conformation. Interrupted base stacking is commonly seen in
185 superfamily I and II helicases and may have an important role in DNA unwinding[8].

186 The platform domain of UL52 is L-shaped and mostly α-helical. The DALI[17] search found
187 no hit with comparable side and Z-score > 6.5, indicating that the PD is likely a novel fold.

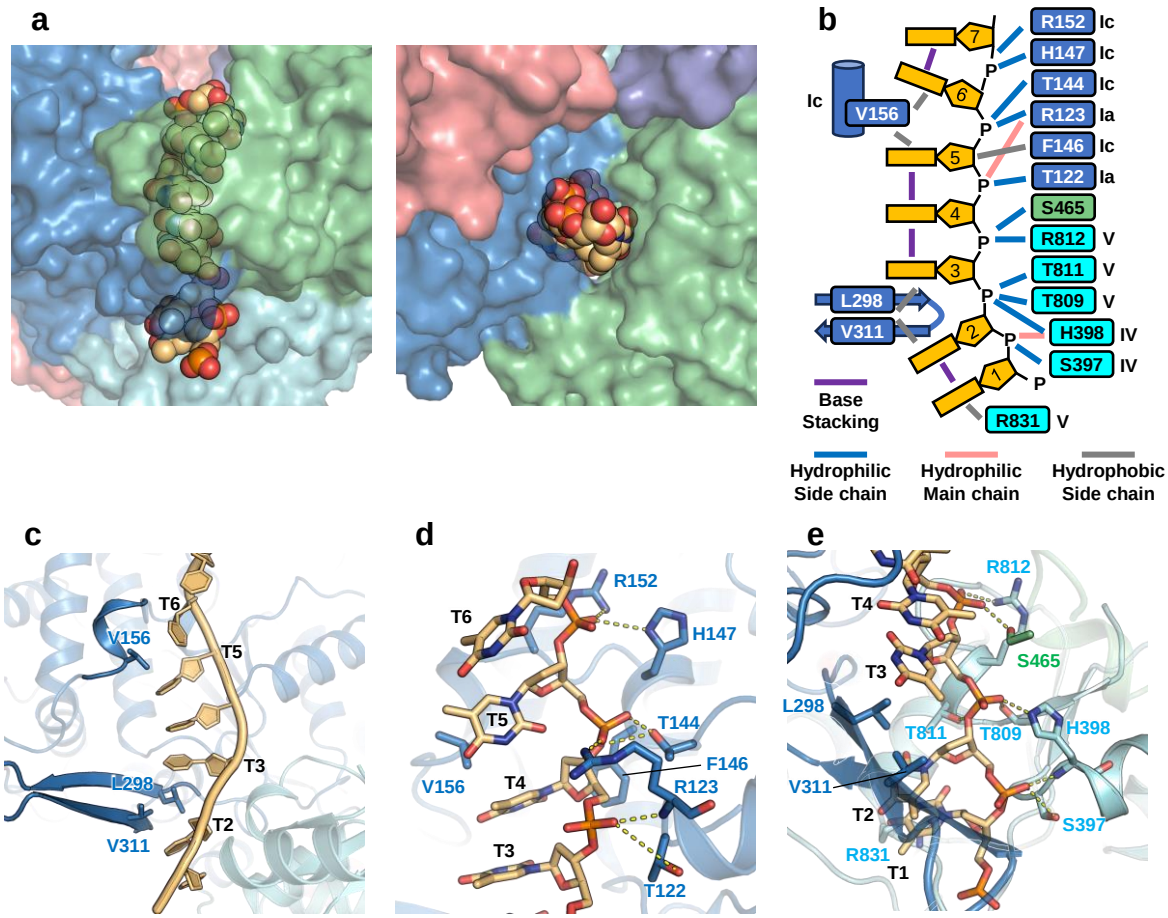

Figure 2: UL5-DNA interaction. a, The bound ssDNA is wrapped by domains 1A, 2A, and 2B (two views). UL5 and ssDNA are shown as a transparent surface model and a sphere model, respectively. **b**, Schematic representation of ssDNA-UL5 interaction. **c**, Two structural motifs interfering with base-stacking interactions. **d** and **e**, Interactions between ssDNA and domain 1A (**d**) or domain 2A (**e**).

188 The PD interacts with the UL5, with a large interaction area, and with inhibitors (Figure
189 1c).

190 **Domains 1A and 2A adopt an open form in the HPI-bound HPC**

191 During their catalytic cycle, superfamily I helicases undergo conformational changes
192 between an ATP-bound closed form and an ATP-free open form [8,22]. The ATPase site
193 comprises motifs I (also known as P-loop or Walker A motif), Ia, II (also known as DEXX
194 motif or Walker B motif), III, IIIa, V, and VI, which are distributed along the cleft between
195 domains 1A and 2A. ATP binding induces closure of this cleft, resulting in the formation of
196 a functional ATPase site contributed by both domains.

197 To gain insights into the mode of action of HPIs, we compared the current AMNV-bound
198 HPC structure with that of the structurally most related helicase, Pif1[20]. In both the AMNV-
199 bound HPC and the open form of Pif1, motifs Ia (domain 1A) and IV (domain 1B) contact
200 the bound ssDNA phosphates that are separated by three nucleotides (Figure 3a, b). In
201 contrast, in the closed form of Pif1, the distance between these motifs corresponds to two
202 nucleotides (Figure 3c). This structural comparison clearly shows that the current HPC
203 structures represent an open form. Since the structure of ATP-free HPC in the absence of
204 HPIs has not yet been determined, it remains unclear how closely the current HPI-bound
205 structures resemble the functional ATP-free form in the catalytic cycle.

206 We also compared the conformations of the ATPase site among the three structures (Figure
207 3d-f). In the closed form of Pif1, the bound ATP analog (ADP-AlF_4^-) is surrounded by
208 residues from both domains 1A and 2A, including residues from motifs I (K97, contacting

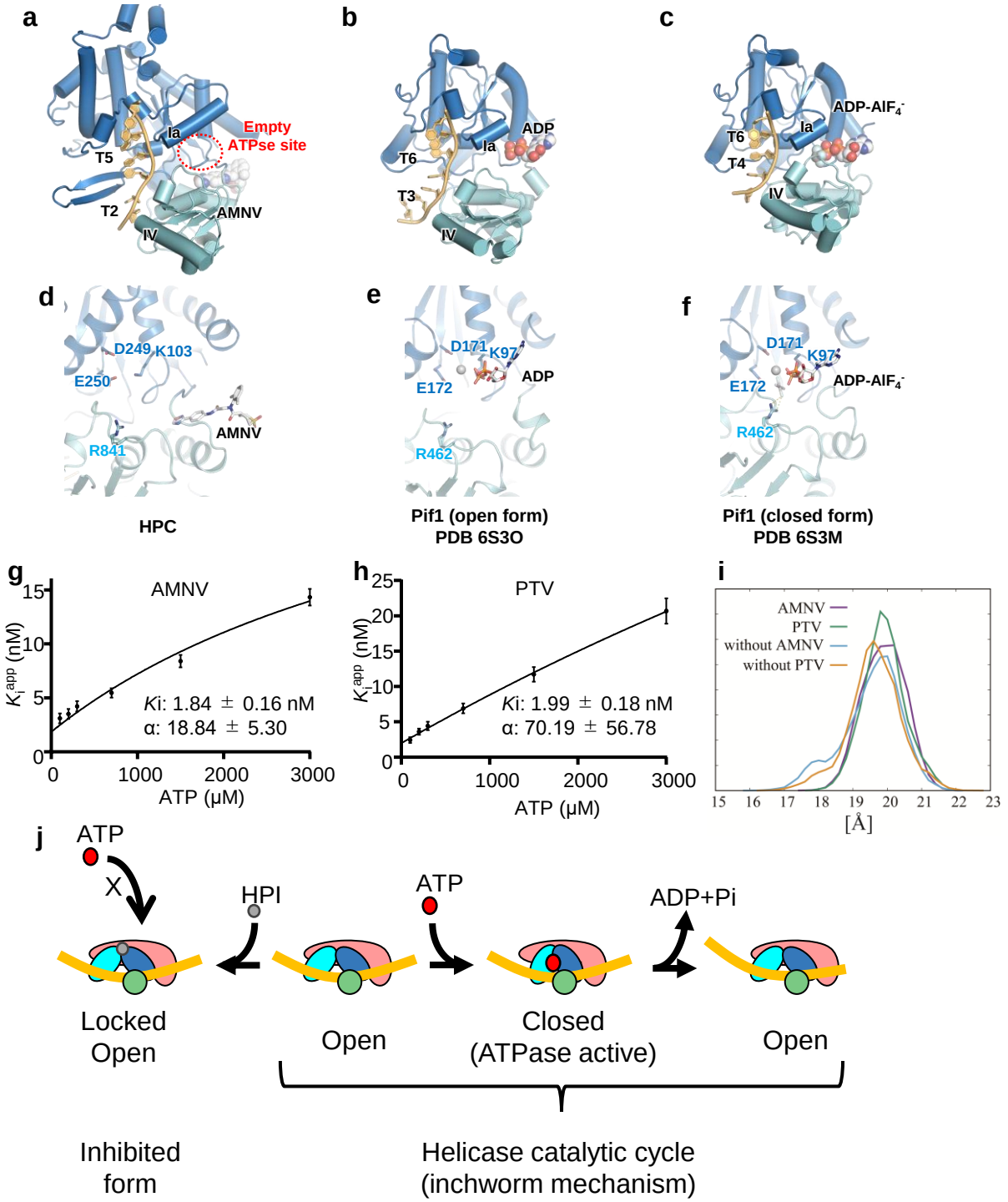

Figure 3: HPIs lock UL5 in an open conformation. .**a**-**c**, Structures of domains 1A and 2A in the ssDNA-bound states of the AMNV-bound HPC (**a**), ADP-bound Pif1 (**b**), and ATP analog-bound Pif1 (**c**). DNA nucleotides contacted by conserved residues in motifs Ia and IV (T122 and S397 of UL5 and their equivalents) are labeled. **d**-**f**, Close-up views of the ATPase site in the AMNV-bound HPC (**d**), ADP-bound Pif1 (**e**), and ATP analog-bound Pif1 (**f**). **g**, **h**, Relationship between ATP concentration and apparent inhibition constant (K_i^{app}), along with their standard error of the mean (SEM), in ATPase inhibition assays of AMNV (**g**) and PTV (**h**). The corresponding *Ki* and α values with SEM are also shown. **i**, Distribution of the distance between the centers of mass of K103, D249, and E250 in domain 1A and R841 in domain 2A during MD simulations. **j**, Proposed model for the inhibition mechanism of HPIs.

209 phosphates), II (D171 and E172, chelating Mg^{2+}), and VI (R462, contacting the γ-phosphate
210 analog). In contrast, in the open form of Pif1, the two domains are separated, and the side
211 chain of R462 is too distant to contact the phosphate groups of the ADP bound to domain
212 1A. Similarly, in the AMNV-bound HPC structures, the corresponding catalytic residues
213 from motifs I (K103), II (D249 and E250), and VI (R841) are also too far apart to
214 coordinate ATP binding. Notably, although 1 mM AMP-PNP was added to the cryo-EM
215 samples, no density was observed at the ATPase site, suggesting that the current open form
216 of HPC has reduced affinity for ATP.

217 **HPIs allosterically and competitively inhibit ATP binding**

218 The open conformation observed in the HPI-bound HPC structures, along with the absence
219 of AMP-PNP density at the ATPase site, suggests that HPI binding alters the conformation
220 of the HPC, thereby allosterically reducing its affinity for ATP. To test this hypothesis, we
221 performed ATPase inhibition assays (Extended Data Figure 9) using varying concentrations
222 of ATP and HPIs, and measured the effect of ATP concentration on the apparent inhibition
223 constant (K_i^{app}). As shown in Figure 3g and h, increasing ATP concentrations led to a
224 corresponding increase in K_i^{app}, suggesting that ATP and HPI binding are reciprocally
225 inhibiting with each other with respect to HPC affinity. We analyzed the inhibition data
226 assuming a mixed inhibition model, in which HPIs can bind both to the free HPC and to the
227 HPC–ATP complex[31]. From this analysis, we calculated the α factor, which represents how
228 differently inhibitors bind to the free HPC versus the HPC–ATP complex. Curve fitting
229 yielded large α factor values for both inhibitors (about 19 for AMNV and 70 for PTV),

230 indicating that both inhibitors bind to the free enzyme much more strongly, acting in a
231 nearly ATP-competitive manner, despite binding at the allosteric site.

232 **HPIs lock the HPC in the open form**

233 Our structural and biochemical analyses suggest that HPIs affect the conformational
234 dynamics of the HPC by locking it in the open conformation observed in our cryo-EM
235 structures. To further substantiate our findings, we performed molecular dynamics (MD)
236 simulations on the following four systems (Extended Data Figure 10a). The first two
237 systems consist of the UL5-UL52 subcomplex bound to ssDNA, with either AMNV or PTV
238 (based on the AMNV- or PTV-bound HPC structures, respectively). The remaining two
239 systems are identical to the first two, but lack the inhibitors, serving as cotrols.

240 For each system, we conducted eight replica MD simulations, each lasting 3 μs, and
241 analyzed the distance between key catalytic residues in domains 1A and 2A: K103, D249,
242 and E250 from motifs I and II in domain 1A, and R841 from motif VI in domain 1B
243 (Figure 3d). As shown in Figure 3i, the HPI-bound systems exhibited a unimodal
244 distribution of inter-residue distances, peaking around 20 Å. In contrast, the HPI-free
245 systems showed a bimodal distribution with peaks centered at approximately 18 Å and 19.5
246 Å. These results suggest that, in the absence of HPIs, domains 1A and 2A undergo
247 spontaneous conformational fluctuations that may potentially facilitate productive ATP
248 binding and hydrolysis. In contrast, HPI binding appears to restrict this flexibility,
249 stabilizing the HPC in an open, catalytically inactive conformation.

250 Based on these findings, we propose the following inhibition model (Figure 3j). In the
251 catalytic cycle of the inchworm model, the helicase alternates between open and closed
252 conformations, driven by ATP binding and hydrolysis. However, upon HPI binding, the
253 HPC is locked in the open conformation, thereby preventing ATP binding and stalling the
254 catalytic cycle. Consequently, the helicase remains inactive and unable to unwind DNA.

255 **Binding and specificity of HPIs**

256 Figure 4a-c shows the interactions between AMNV and PTV with the HPC, respectively. In
257 both complexes, two connected aromatic rings of each HPI are surrounded by residues
258 N98, N343, G352, M355, and K356 of UL5, as well as Y356 of UL52. AMNV and PTV
259 contain two and one carbonyl group(s), respectively, in their central regions, which are
260 within hydrogen-bonding distance of the UL5 K356 side chain. A sulfonyl group, which is
261 shared by both HPIs, forms a hydrogen bond with the side chain of UL52 N902. The
262 dimethylphenyl group, unique to AMNV, engages in hydrophobic interactions with the side
263 chains of UL5 Y882 and UL52 F360. Most of the known single-point resistance mutations
264 of AMNV (G352C, M355T, and K356N in UL5, as well as F360V/C and N902T in
265 UL52)[32] and PTV (N342K, G352V, M355T, and K356Q in UL5 as well as A899T in
266 UL52)[14,33,34] are located at or near the binding site, directly accounting for their resistance
267 mechanisms. Although the HPI-contacting residues in UL5 are well conserved among all
268 human herpesviruses, those in UL52, such as F360, A899, N902, H906, and F907, are less
269 conserved (Figure 4d). This observation explains why the current HPIs are ineffective

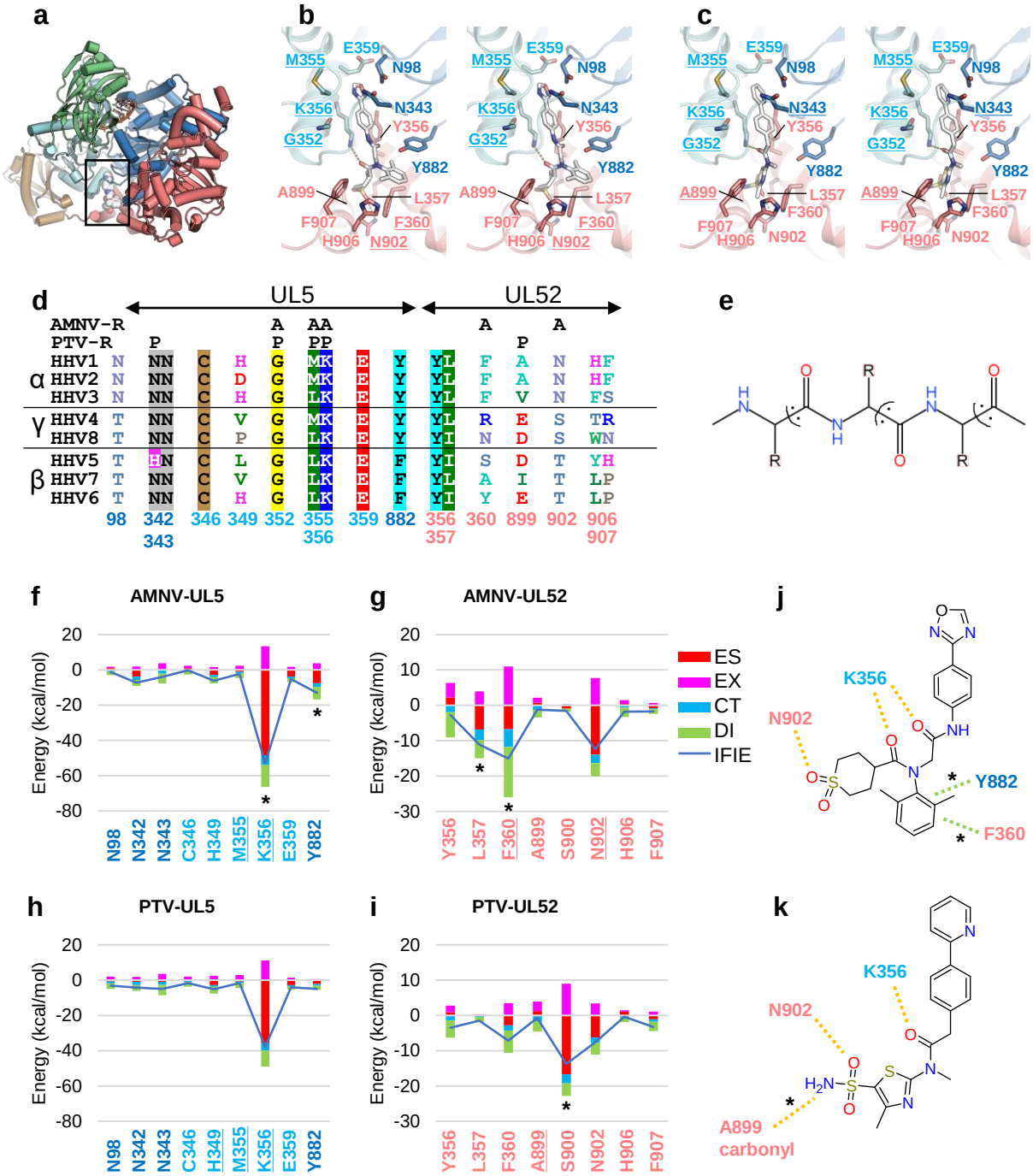

Figure 4: Binding and specificity of HPIs. a, Overall structure of the HPC, with the HPI binding site highlighted by a box. **b, c**, Stereo views of the binding site for AMNV (**b**) and PTV (**c**). Residues associated with resistance mutations are underlined. **d**, Sequence alignment of residues involved in HPI binding. “A” and “P” denote mutations that confer resistance to AMNV and PTV, respectively. **e**, Fragmentation scheme used for FMO calculations. **f–i**, PIEDA results showing interactions between AMNV and UL5 (**f**), AMNV and UL52 (**g**), PTV and UL5 (**h**), and PTV and UL52 (**i**). ES, EX, CT, and DI refer to the electrostatic, exchange-repulsion, charge transfer with higher-order mixing, and dispersion terms, respectively. Asterisks indicate residues contributing more than 5 kcal/mol to binding in one complex compared to the other. **j, k**, Schematic representations of the interactions between the HPC and AMNV (**j**) or PTV (**k**).

270 against β- and γ-herpesviruses and provides a structural basis for the rational design of
271 novel HPIs targeting these subfamilies.

272 We next analyzed the MD trajectories to assess the potential contribution of water
273 molecules to the HPI binding. As shown in Extended Data Figure 10b and c, a region of
274 high water density was observed in both complexes, where two water molecules bridge the
275 side chain of UL5 K356 and the sulfonyl group of the HPIs. Notably, these bridging water
276 molecules connect UL5 K356 and the sulfonyl group for 39.1% and 45.0% of the
277 simulation time in the AMNV and PTV complexes, respectively, suggesting the formation
278 of a stable hydrogen-bonding network. This water-mediated interaction may explain why
279 the sulfonyl group is essential for the tight binding of these inhibitors.

280 To quantitatively evaluate the differences between the AMNV and PTV-bound structures
281 and to gain mechanistic insights into their distinct anti-herpesvirus spectra, we performed
282 fragment molecular orbital (FMO) calculation analysis[35–38] on the representative structures
283 of MD trajectories. The FMO method divides biological macromolecules into residue-
284 based fragments (Figure 4e), thereby accelerating quantum chemical calculations and
285 enabling the extraction of inter-fragment interaction energy (IFIE) and its decomposition
286 data. To account for structural fluctuations in the HPI-HPC interactions, we clustered the
287 MD trajectories into four groups based on the coordinates of the HPI binding site (Extended
288 Data Figure 10d), performed FMO calculations on the representative structures, and
289 calculated the weighted average energies, taking into account the existence probabilities of
290 each cluster.

291 Figure4f-i summerizes the FMO analysis results, showing the frequency-weighted average
292 values of IFIE and pair interaction energy decomposition analysis (PIEDA)[39] between
293 either AMNV or PTV and the UL5 and UL52 subunits. In agreement with our manual
294 inspection, residues involved in recognizing the common structural features of the two
295 HPIs are consistently identified in both complexes. These include residues surrounding the
296 two connected aromatic rings (UL5 N98, N343, and M355), UL5 K356 forming hydrogen
297 bonds with the HPIs' carbonyl oxygen, and UL52 N902 forming a hydrogen bond with the
298 sulfonyl oxygen.

299 In addition, comparison of the IFIE and PIEDA data reveals distinct binding features of
300 AMNV and PTV (Figure 4j, k). The stronger attractive interaction energies for UL5 Y882
301 and UL52 F360 in the AMNV complex (by approximately 8.1 and 7.9 kcal/mol,
302 respectively), consisting of considerable dispersion interaction energy (Figure 4f-i),
303 indicate that the recognition of AMNV's unique dimethylphenyl group by these residues
304 via π-π and CH/π interactions, respectively (Figure 4b), substantially contributes to the
305 binding affinity. Notably, these residues are conserved across the α-subfamily, consistent
306 with the AMNV's broad efficacy against all α-subfamily members (Figure 4d). In contrast,
307 UL52 S900 exhibits a stronger IFIE value in the PTV complex, mainly due to electrostatic
308 and charge transfer interactions, suggesting the presence of the hydrogen bond[38]. In the
309 FMO method, proteins are fragmented between the α-carbon and carbonyl carbon,
310 assigning the carbonyl group to the next residue (+1) (Figure 4e). Structural analysis of the
311 PTV complex revealed a hydrogen bond between the A899 carbonyl group (assigned as
312 S900 in the FMO scheme) and the PTV-specific NH_2 group of the sulfonamide moiety

313 (Extended Data Figure 11a). Structural modeling suggests that the substitution of A899
314 with threonine (which confers PTV resistance) or with valine (the corresponding residue in
315 HHV3, Figure 4d) introduces steric hinderance that disrupts this interaction (Extended Data
316 Figure 11b, c). Moreover, the A899T substitution does not confer resistance to BILS 22 BS,
317 another HPI that retains a sulfonyl group but lacks the NH_2 group[34]. Collectively, these
318 findings indicate that the unique hydrogen bond between the NH_2 group of PTV and the
319 A899 carbonyl oxygen is critical for its inhibitory activity, and explain PTV's limited
320 activity against HHV3.

321 **Discussion**

322 Our structural, biochemical, and computational analyses collectively elucidate the
323 mechanism of action of AMNV and PTV and shed light on why these HPIs are less
324 effective against the β- and γ-herpesvirus subfamilies. Moreover, our MD and FMO
325 analyses clarify how a small difference in the chemical structures of AMNV and PTV
326 results in distinct anti-herpesvirus spectra within the α-subfamily. Together, these findings
327 establish a structural framework for the rational design of novel HPIs with tailored anti-
328 herpesvirus spectrum and/or improved pharmacokinetic properties.

329 Structures solved by cryo-EM often lack information on conformational dynamics, and may
330 suffer from limited resolution, leading to uncertainty in positioning of ligands and
331 surrounding water molecules. To overcome these limitations, we performed molecular
332 dynamics (MD) simulations to capture structural fluctuations and water behavior, followed
333 by FMO analysis to quantitatively evaluate molecular interactions. This integrated

approach provided in-depth insights into HPI–HPC interactions that aligned well with previous mutational studies, supporting the reliability of our methodology. The combined use of MD and FMO thus represents a powerful framework for investigating systems where structural data alone is insufficient to fully characterize essential molecular interactions[40,41].

Helicases, which play essential roles in nearly all aspects of nucleic acid metabolism, have long been recognized as promising drug targets. However, developing effective helicase inhibitors has proven challenging, likely due to the chemical nature of the ATP- and nucleic acid-binding sites, which are difficult to target with small molecules[42,43]. Recent studies have reported the development of specific helicase inhibitors that act allosterically[44–46]. In this study, we demonstrate that AMNV and PTV, two clinical inhibitors, bind to a shared allosteric pocket at the interface between the helicase subunit (UL5) and the non-helicase subunit (UL52). Our detailed characterization of these clinical HPIs, which act allosterically yet competitively, provides valuable insights for the development of diverse inhibitors targeting helicases from a wide range of sources, including both cellular and pathogenic origins.

The current HPC structures shed light on the coupling mechanism between DNA unwinding and primer synthesis; however, several questions remain unresolved. Do UL5 and UL52 engage with a single continuous ssDNA strand? How do the HM and PM reposition themselves during the catalytic cycle? Does the ZBD participate in binding the ssDNA template to facilitate efficient primer synthesis by the PD? To address these questions and elucidate the coupling mechanism, it will be necessary to determine the

355 structures of HPC actively engaged in both DNA unwinding and primer synthesis in both
356 ATP-bound and ATP-free states. Such structural insights will also be valuable for deepening
357 our understanding of DNA replication mechanisms across diverse organisms.

358

359 **Methods**

360 **Protein expression and purification**

361 Full-length coding sequences of HHV-1 UL5, UL52, and UL8 were synthesized by Twist
362 Bioscience and individually cloned into the pACEBac1 vector. An N-terminal twin-strep–
363 His tag was fused to UL5, while N-terminal His–SUMOstar tags were fused to UL52 and
364 UL8. Baculoviruses were generated in Sf9 cells using the Bac-to-Bac system (Thermo
365 Fisher Scientific) according to the manufacturer's protocol. The HPC was reconstituted by
366 co-infecting Sf9 cells with the three respective recombinant baculoviruses at a multiplicity
367 of infection of 3:3:3. Cells were harvested 48 hours post-infection.

368 Cell pellets were resuspended in lysis buffer (100 mM Tris-HCl (pH 8.0), 150 mM NaCl,
369 1 mM $MgCl_2$, 0.5 mM TCEP, 0.5% Tween 20, 10% glycerol, 0.1 mM PMSF, and cOmplete
370 ULTRA protease inhibitor cocktail (Roche)) and lysed by sonication. The clarified lysate
371 was loaded onto a Strep-Tactin XT 4Flow column (IBA Lifesciences), and the bound
372 protein complex was eluted with buffer containing 20 mM Tris-HCl (pH 8.0), 500 mM
373 NaCl, 10% glycerol, 0.5 mM TCEP, and 50 mM D-biotin. The eluate was subsequently
374 applied to a HisTrap HP column (Cytiva) and eluted with buffer containing 20 mM Tris-
375 HCl (pH 8.0), 500 mM NaCl, 10% glycerol, 0.5 mM TCEP, and 500 mM imidazole. The

376 eluted sample was dialyzed against buffer A (20 mM Tris-HCl (pH 8.0), 150 mM NaCl,
377 0.5 mM TCEP) and concentrated for cryo-EM sample preparation.

378 For tag removal, the HisTrap eluate was mixed with SUMOstar protease and HRV 3C
379 protease and dialyzed against buffer A. The sample was subsequently passed through a
380 HisTrap column to remove cleaved tags and proteases. The flow-through containing tag-
381 free HPC was further dialyzed against buffer A, concentrated, flash-frozen in liquid
382 nitrogen, and stored at −80 °C for ATPase assays.

383 **Cryo-EM sample preparation**

384 For grid preparation of the AMNV-bound complex, 0.4 μM tagged HPC was mixed with 4
385 μM 43-mer ssDNA (5'-TTTTTTTTTCCTGTTTTTTTTTTTTTTTTTTTTTTTTTTTTTT-
386 3'; Fasmac), 1 mM AMP-PNP, 10 mM $MgCl_2$, and 100 μM AMNV (AstaTech), and then
387 concentrated 10-fold. For the PTV-bound complex, 0.48 μM tagged HPC was mixed with
388 4.8 μM 43-mer ssDNA, 1 mM AMP-PNP, 10 mM $MgCl_2$, and 100 μM PTV (Selleck), and
389 then concentrated 7.6-fold. Concentration was performed using a Vivaspin 500 device
390 (MWCO 50 kDa; Sartorius).

391 Due to orientation bias observed on Au 300-mesh R1.2/1.3 grids, the samples were applied
392 to freshly glow-discharged Au 300-mesh R0.6/1 holey carbon grids (Quantifoil), pre-treated
393 with 3 μL of amylamine to mitigate bias[47]. The grids were blotted for 4 s at 4 °C under
394 100% humidity and plunge-frozen in liquid ethane using a Vitrobot Mark IV (Thermo
395 Fisher Scientific).

396 **Cryo-EM data acquisition and processing**

397 Cryo-EM data were collected using a Titan Krios G4 transmission electron microscope
398 (Thermo Fisher Scientific) operated at 300 kV, equipped with a K3 direct electron detector
399 (Gatan), installed at the University of Tokyo. Data acquisition was performed using EPU
400 v3.4.0.5704, with a defocus range of −0.6 to −1.6 μm. Data acquisition statistics are
401 summarized in Supplementary Table 1.

402 The cryo-EM data were processed using CryoSPARC v4.4.1[48] (Extended Data Figures 1
403 and 2). For the AMNV complex, an initial dataset of 803 micrographs was used for blob
404 picking, 2D classification, and template generation. These templates were then applied to
405 the main dataset of 12,466 micrographs for template-based particle picking, followed by
406 neural network-based picking using Topaz[49]. Subsequent reconstruction and refinement
407 yielded a global map with poorly resolved density in the HM. Following 3D classification
408 without a focus mask, seven out of ten classes were selected, which showed slightly
409 improved HM density. Particles corresponding to the HM and PM were then subtracted and
410 used for local refinement. The global map was further refined using 3DFlex[16].

411 For the PTV complex, data were processed similarly to the AMNV dataset. However, the
412 AMNV-derived templates were reused for template-based particle picking, and no particle
413 subtraction was performed.

414 **Model building and refinement**

415 The initial model of the HPC was generated using LocalColabFold[50], which employs
416 AlphaFold2[51] for structure prediction, and was fitted into the cryo-EM map. The predicted
417 model showed good overall agreement with the map, although notable differences were

418 observed in local loop regions (including the HPIs binding pocket) and in the relative
419 orientation between the HM and PM. The model was manually adjusted using Coot
420 v0.9.8.93[52] and further refined with the *phenix.real_space_refine* module in Phenix
421 v1.21.1-5286[53]. No map sharpening was applied. To build the atomic models of the HPIs,
422 multiple conformations of their functional groups (the oxadiazole ring of AMNV, and the
423 pyridine ring and NH_2 group of PTV) were generated and evaluated using FMO
424 calculations. The conformation with the lowest energy was then selected. Structural figures
425 were prepared using PyMOL v2.5.0 (Schrödinger, LLC) and ChimeraX v1.9[54]. Data
426 processing and refinement statistics are summarized in Supplementary Table 2.

427 **ATPase assay**

428 ATPase activity was assessed using an NADH-coupled microplate assay as previously
429 described[55], performed over a 30-minute time course at 30 °C, with absorbance
430 measurements taken every 30 seconds. Each 54 µL reaction was prepared in ATPase buffer
431 containing 20 mM HEPES-NaOH (pH 7.5), 5 mM $MgCl_2$, 10% glycerol, 5 mM TCEP,
432 100 µg/mL bovine serum albumin, 2 µM 43-mer ssDNA, 3 mM phosphoenolpyruvate
433 (Nacalai Tesque), 1 mM NADH (Sigma-Aldrich), 1% DMSO, 0.02 U/µL L-lactate
434 dehydrogenase (Sigma-Aldrich), 0.02 U/µL pyruvate kinase (Sigma-Aldrich), 10 nM tag-
435 free HPC, and ATP (Nacalai Tesque) at final concentrations of 0, 0.1, 0.2, 0.3, 0.7, 1.5, or
436 3 mM. Either AMNV or PTV was added separately at concentrations of 0, 2.5, 5, 10, 15,
437 20, or 25 nM. Reactions were dispensed into a 96-well half-area microplate (Greiner Bio-
438 One), and NADH oxidation was monitored by measuring absorbance at 340 nm using a

439 Tecan Spark Cyto 400 multimode microplate reader. Reaction velocities (v, OD/sec) were
440 determined from the linear portion of the absorbance decrease at 340 nm between 1000 and
441 1500 seconds. Background signals measured in the absence of ATP were subtracted to
442 correct the data. The Michaelis constant (K_M) was determined by non-linear fitting to the
443 Michaelis–Menten equation using GraphPad Prism v10.2.3 (GraphPad Software).

444 Both AMNV and PTV exhibited EC_{50} values of less than 100 nM against the virus [12,14],
445 indicating their behavior as tight-binding inhibitors [31,56]. The apparent inhibition constant
446 (K_i^{app}) was determined by non-linear fitting to the Morrison equation (Eq. 1), where v_i is the
447 initial rate of the inhibited reaction, v_0 is the initial rate of the uninhibited reaction, [E] is
448 the enzyme concentration, [I] is the inhibitor concentration, and K_i^{app} is the apparent
449 inhibition constant [31,56].

450 $$v_i = v_0\left(1 - \frac{([E]+[I]+K_i^{app}) - \sqrt{([E]+[I]+K_i^{app})^2 - 4[E][I]}}{2[E]}\right) \qquad \text{(Eq. 1)}$$

451 The K_i^{app} values were plotted against ATP concentrations and fitted by non-linear regression
452 to a mixed inhibition model (Eq. 2), in which [S] represents the ATP concentration, K_M is
453 the Michaelis constant, α reflects the difference in inhibitor affinity for the free enzyme
454 versus the enzyme-substrate complex, and K_i is the inhibition constant [31,56]. This analysis
455 yielded values for α and K_i.

456 $$K_i^{app} = \frac{[S]+K_M}{\frac{K_M}{K_i}+\frac{[S]}{\alpha K_i}} \qquad \text{(Eq. 2)}$$

457 **Modeling of the UL5–UL52 subcomplex for MD simulations**

458 For UL5, the N-terminal region (M1–A33) and a large C-terminal loop (A582–E657) were
459 excluded from the model. A shorter missing loop (A563–E568) was modeled using
460 MODELLER[57], and the termini adjacent to the large loop (T581, T658) were capped with
461 N-methylamide (NME) and acetyl (ACE) groups, respectively. For UL52, the N- and C-
462 terminal regions (M1–T16, P1044–P1058), as well as a large internal loop (P682–P752),
463 were also excluded. The termini flanking this large loop (R681, V753) were capped in the
464 same manner. Three smaller loops (S170–D183, P481–C498, R995–A996) were modeled
465 with MODELLER by generating 100 loop conformations with the remaining structure held
466 fixed; the lowest-energy models were selected for each. The resulting structure was used
467 for subsequent molecular dynamics simulations.

468 **MD simulations of the UL5–UL52 subcomplexes**

469 We prepared four systems of the UL5–UL52 complex: two containing ligands (AMNV or
470 PTV) and two ligand-free systems generated by removing the respective ligands. MD
471 simulations were performed using the pmemd module in AMBER20[58,59], with force fields
472 ff99SB for protein[60], bsc1 for DNA[61], and ff99ions08 for ions[62]. The force field parameters
473 for ligands were prepared using the Antechamber package[63] in AmberTools and the general
474 Amber force field (GAFF)[64] for organic molecules. A quantum chemical calculation to
475 geometrically optimize the ligands were carried out with HF/6-31G* basis set using
476 Gaussian 03 software[65]. The net charge for each ligand was set at 0. Discrete partial atomic
477 charges were assigned with HF/6-31G* basis set using the Restrained Electrostatic

478 Potential (RESP) fitting method[66]. The zinc AMBER force field (ZAFF) for the 4-
479 coordinated zinc metal centers[67] was used for the zinc ion in the ZBD. The UL5 – UL52
480 complex was solvated in a cubic periodic box of ~ 190 Å × 190 Å × 190 Å , containing ~
481 220,000 TIP3P water molecules[68] and 0.15 M NaCl to mimic physiological ionic strength.
482 The complex was positioned such that all atoms were separated at least 20 Å from the edge
483 of the box. The resulting system contained ~ 690,000 atoms in total.

484 For each of the four systems, the MD simulations were carried out using eight replicas of
485 identical structures, each initiated with different random seeds for velocity assignment.
486 Each replica was run for 3.16 μs, totaling 25.28 μs per system, under constant pressure of
487 one bar and temperature of 300 K. The dielectric constant was set to 1.0 and the van der
488 Waals interactions were calculated with a 9 Å cutoff. Electrostatic interactions were treated
489 using the particle mesh Ewald (PME) method[69], with a charge grid spacing close to 1 Å.
490 The charge grid was interpolated using a fourth-order cubic B-spline with the direct sum
491 tolerance of 10^{-5} at a 9 Å direct space cutoff. Temperature and pressure were regulated by
492 Langevin dynamics with a collision frequency of 2 ps^{-1}; coupling times were set to 1 ps^{-1}
493 for both. Bond lengths involving hydrogen atoms were constrained with the SHAKE
494 algorithm[70,71]. The leap-frog algorithm was used to integrate the equations of motion with a
495 2 fs time step. The system was gradually heated from 0 K to 300 K over 10 ns, during
496 which the solute atoms were restrained with decreasing force constants while water
497 molecules and ions were allowed to move freely. Conformational snapshots were saved
498 every 100 ps. Trajectories from the final 3 μs of each of the eight replicas (totaling 24 μs)

499 were used for analysis. Water density maps were generated using the volmap tool in
500 VMD[72].

501 **K-mean clustering of the MD trajectories**

502 K-means clustering was performed on all atoms in residues located within 3.5 Å of the
503 ligands in the energy-minimized structure. Specifically, these residues were Asn98, Ile341,
504 Asn343, Met355, Lys356, Glu359, Tyr836, and Tyr882 of UL5, and Tyr356, Phe360,
505 Ala899, and Asn902 of UL52. K-means clustering with K = 4 grouped the trajectories for
506 the UL5-UL52 complex with AMNV into four distinct clusters: 10.5%, 40.2%, 42.7%, and
507 6.6% of the total trajectory. For the PTV-bound complex, the corresponding cluster
508 populations were 70.0%, 4.9%, 0.1%, and 25.0%. Representative structures were selected
509 as those closest to the centroids of each cluster. The RMSD values relative to the centroids
510 were 0.659, 0.515, 0.588, and 0.703 Å for the AMNV-bound UL5–UL52 complex, and
511 0.568, 0.555, 0.779, and 0.520 Å for the PTV-bound complex.

512 **FMO calculation and interaction energy analysis**

513 FMO calculations were performed on the representative structures obtained by clustering of
514 MD trajectories. As a preprocessing step, MD representative structures were subjected to
515 energy minimization by applying a positional constraint of 1.0 kcal/mol-$Å^2$ to heavy atoms,
516 and water within 10 Å around the HPC protein, HPI, ssDNA, and ligand was extracted for
517 calculation. Fragmentation was performed by using amino acid residue units for proteins,
518 base and sugar-phosphate fragments for DNA, and single fragments for ligand and water

519 molecules[73]. The FMO calculations were performed at the MP2/6-31G*[74,75] theoretical
520 level using the ABINIT-MP program[76]. The supercomputer Fugaku was used.

521 Defining the inter-fragment interaction energy (IFIE) between fragments i and j as E_{ij}, pair
522 interaction energy decomposition analysis (PIEDA)[39] divides IFIE into four energy
523 components as follows.

524 $E_{ij} = E_{ij}^{ES} + E_{ij}^{EX} + E_{ij}^{CT+mix} + E_{ij}^{DI}$ (Eq 3)

525 In this study, *i* is HPI (AMNV or PTV), and *j* is each residue of HPC. Weighted average
526 IFIE/PIEDA, E_{ij}^{weight}, is the sum of the interaction energies between HPI and each residue
527 in the cluster representative structure, weighted by the occurrence frequency of each cluster.

528 $E_{ij}^{weight} = \sum_{\alpha} w_{\alpha} E_{ij}^{\alpha}$ (Eq.4)

529 Here, w_{α} is the weight of cluster α, which is 0.105, 0.402, 0.427, and 0.066 for AMNV, and
530 0.700, 0.049, 0.001, and 0.250 for PTV. Figure 4f-i shows the weighted average interaction
531 energy calculated using Eq. 4.

532 Cryo-EM structures were also evaluated using MP2/6-31G* level FMO calculations. For
533 preprocessing of the structures, hydrogen atoms were added and energy minimization was
534 performed using Amber10:EHT force field.

535

536 **Data availability**

537 Coordinates and density maps have been deposited in Protein Data Bank (accession codes
538 9UT1, 9UT3, 9UT4, 9UT5, 9UT6, and 9UT7) and Electron Microscopy Data Bank
539 (accession codes EMD-64478, EMD-64479, EMD-64480, EMD-64481, EMD-64482, and
540 EMD-64483), respectively. FMO data will be deposited in FMODB[77] (accession codes
541 #### and ####).

542 **References**

543 1. *Human Herpesviruses: Biology, Therapy, and Immunoprophylaxis*. (Cambridge
544 University Press, Cambridge ; New York, 2007).

545 2. Marcocci, M. E. *et al.* Herpes Simplex Virus-1 in the Brain: The Dark Side of a
546 Sneaky Infection. *Trends Microbiol.* **28**, 808–820 (2020).

547 3. Eyting, M. *et al.* A natural experiment on the effect of herpes zoster vaccination
548 on dementia. *Nature* 1–9 (2025) doi:10.1038/s41586-025-08800-x.

549 4. Bjornevik, K., Münz, C., Cohen, J. I. & Ascherio, A. Epstein–Barr virus as a
550 leading cause of multiple sclerosis: mechanisms and implications. *Nat. Rev. Neurol.*
551 **19**, 160–171 (2023).

552 5. Mozhgani, S.-H. *et al.* Human Herpesvirus 6 Infection and Risk of Chronic
553 Fatigue Syndrome: A Systematic Review and Meta-Analysis. *Intervirology* **65**, 49–57
554 (2021).

555 6. Bermek, O. & Williams, R. S. The three-component helicase/primase complex
556 of herpes simplex virus-1. *Open Biol.* **11**, 210011 (2021).

557 7. Fernandez, A. J. & and Berger, J. M. Mechanisms of hexameric helicases. *Crit.*
558 *Rev. Biochem. Mol. Biol.* **56**, 621–639 (2021).

559 8. Fairman-Williams, M. E., Guenther, U.-P. & Jankowsky, E. SF1 and SF2
560 helicases: family matters. *Curr. Opin. Struct. Biol.* **20**, 313–324 (2010).

561 9. Saikrishnan, K., Powell, B., Cook, N. J., Webb, M. R. & Wigley, D. B. Mechanistic
562 Basis of 5'-3' Translocation in SF1B Helicases. *Cell* **137**, 849–859 (2009).

563 10. Bergsch, J., Allain, F. H.-T. & Lipps, G. Recent advances in understanding
564 bacterial and archaeoeukaryotic primases. *Curr. Opin. Struct. Biol.* **59**, 159–167
565 (2019).

566 11. Shiraki, K., Yasumoto, S., Toyama, N. & Fukuda, H. Amenamevir, a Helicase-
567 Primase Inhibitor, for the Optimal Treatment of Herpes Zoster. *Viruses* **13**, 1547
568 (2021).

569 12. Chono, K. *et al.* ASP2151, a novel helicase-primase inhibitor, possesses
570 antiviral activity against varicella-zoster virus and herpes simplex virus types 1 and 2.
571 *J. Antimicrob. Chemother.* **65**, 1733–1741 (2010).

572 13. Ohtsu, Y., Susaki, Y. & Noguchi, K. Absorption, Distribution, Metabolism, and
573 Excretion of the Novel Helicase-Primase Inhibitor, Amenamevir (ASP2151), in
574 Rodents. *Eur. J. Drug Metab. Pharmacokinet.* **43**, 693–706 (2018).

575 14. Kleymann, G. *et al.* New helicase-primase inhibitors as drug candidates for the
576 treatment of herpes simplex disease. *Nat. Med.* **8**, 392–398 (2002).

577 15. Birkmann, A. *et al.* Discovery, Chemistry, and Preclinical Development of
578 Pritelivir, a Novel Treatment Option for Acyclovir-Resistant Herpes Simplex Virus
579 Infections. *J. Med. Chem.* **65**, 13614–13628 (2022).

580 16. Punjani, A. & Fleet, D. J. 3DFlex: determining structure and motion of flexible
581 proteins from cryo-EM. *Nat. Methods* **20**, 860–870 (2023).

582 17. Holm, L., Laiho, A., Törönen, P. & Salgado, M. DALI shines a light on remote
583 homologs: One hundred discoveries. *Protein Sci.* **32**, e4519 (2023).

584 18. Chen, W.-F. *et al.* Crystal structures of the BsPif1 helicase reveal that a major
585 movement of the 2B SH3 domain is required for DNA unwinding. *Nucleic Acids Res.*
586 **44**, 2949–2961 (2016).

587 19. Zhou, X. *et al.* Structural and Functional Insights into the Unwinding
588 Mechanism of *Bacteroides sp* Pif1. *Cell Rep.* **14**, 2030–2039 (2016).

589 20. Dai, Y.-X. *et al.* Structural and functional studies of SF1B Pif1 from *Thermus*
590 *oshimai* reveal dimerization-induced helicase inhibition. *Nucleic Acids Res.* **49**, 4129–
591 4143 (2021).

592 21. Lu, K.-Y. *et al.* Structural study of the function of *Candida Albicans* Pif1.
593 *Biochem. Biophys. Res. Commun.* **567**, 190–194 (2021).

594 22. Velankar, S. S., Soultanas, P., Dillingham, M. S., Subramanya, H. S. & Wigley, D.
595 B. Crystal Structures of Complexes of PcrA DNA Helicase with a DNA Substrate
596 Indicate an Inchworm Mechanism. *Cell* **97**, 75–84 (1999).

597 23. Li, A. W. H. *et al.* Molecular basis for the initiation of DNA primer synthesis.
598 *Nature* **605**, 767–773 (2022).

599 24. Chen, Y. *et al.* Herpes Simplex Virus Type 1 Helicase-Primase: DNA Binding and
600 Consequent Protein Oligomerization and Primase Activation. *J. Virol.* **85**, 968–978
601 (2011).

602 25. David, A., Islam, S., Tankhilevich, E. & Sternberg, M. J. E. The AlphaFold
603 Database of Protein Structures: A Biologist's Guide. *J. Mol. Biol.* **434**, 167336 (2022).

604 26. Keen, B. A., Jozwiakowski, S. K., Bailey, L. J., Bianchi, J. & Doherty, A. J.
605 Molecular dissection of the domain architecture and catalytic activities of human
606 PrimPol. *Nucleic Acids Res.* **42**, 5830–5845 (2014).

607 27. Kazlauskas, D. & Venclovas, Č. Herpesviral helicase-primase subunit UL8 is
608 inactivated B-family polymerase. *Bioinformatics* **30**, 2093–2097 (2014).

609 28. Muylaert, I., Zhao, Z., Andersson, T. & Elias, P. Identification of Conserved
610 Amino Acids in the Herpes Simplex Virus Type 1 UL8 Protein Required for DNA
611 Synthesis and UL52 Primase Interaction in the Virus Replisome *. *J. Biol. Chem.* **287**,
612 33142–33152 (2012).

613 29. Zhu, L. A. & Weller, S. K. The six conserved helicase motifs of the UL5 gene
614 product, a component of the herpes simplex virus type 1 helicase-primase, are
615 essential for its function. *J. Virol.* **66**, 469–479 (1992).

616 30. Graves-Woodward, K. L., Gottlieb, J., Challberg, M. D. & Weller, S. K.
617 Biochemical Analyses of Mutations in the HSV-1 Helicase-Primase That Alter ATP
618 Hydrolysis, DNA Unwinding, and Coupling Between Hydrolysis and Unwinding. *J. Biol.*
619 *Chem.* **272**, 4623–4630 (1997).

620 31. Copeland, R. A. *Enzymes: A Practical Introduction to Structure, Mechanism,*
621 *and Data Analysis*. (Wiley, 2000). doi:10.1002/0471220639.

622 32. Sato, Y. *et al*. Characteristics of Helicase-Primase Inhibitor Amenamevir-
623 Resistant Herpes Simplex Virus. *Antimicrob. Agents Chemother.* **65**, e00494-21
624 (2021).

625 33. Biswas, S., Miguel, R. N., Sukla, S. & Field, H. J. A mutation in helicase motif IV
626 of herpes simplex virus type 1 UL5 that results in reduced growth in vitro and lower
627 virulence in a murine infection model is related to the predicted helicase structure. *J.*
628 *Gen. Virol.* **90**, 1937–1942 (2009).

629 34. Biswas, S. *et al*. A single drug-resistance mutation in HSV-1 UL52 primase
630 points to a difference between two helicase–primase inhibitors in their mode of
631 interaction with the antiviral target. *J. Antimicrob. Chemother.* **61**, 1044–1047 (2008).

632 35. Fedorov, D. G., Nagata, T. & Kitaura, K. Exploring chemistry with the fragment
633 molecular orbital method. *Phys. Chem. Chem. Phys.* **14**, 7562 (2012).

634 36. Kitaura, K., Ikeo, E., Asada, T., Nakano, T. & Uebayasi, M. Fragment molecular
635 orbital method: an approximate computational method for large molecules. *Chem.*
636 *Phys. Lett.* **313**, 701–706 (1999).

637 37. Tanaka, S., Mochizuki, Y., Komeiji, Y., Okiyama, Y. & Fukuzawa, K. Electron-
638 correlated fragment-molecular-orbital calculations for biomolecular and nano
639 systems. *Phys Chem Chem Phys* **16**, 10310–10344 (2014).

640 38. Fukuzawa, K. & Tanaka, S. Fragment molecular orbital calculations for
641 biomolecules. *Curr. Opin. Struct. Biol.* **72**, 127–134 (2022).

642 39. Fedorov, D. G. & Kitaura, K. Pair interaction energy decomposition analysis. *J.*
643 *Comput. Chem.* **28**, 222–237 (2007).

644 40. Handa, Y. *et al*. Prediction of Binding Pose and Affinity of Nelfinavir, a SARS-
645 CoV-2 Main Protease Repositioned Drug, by Combining Docking, Molecular
646 Dynamics, and Fragment Molecular Orbital Calculations. *J. Phys. Chem. B* **128**, 2249–
647 2265 (2024).

648 41. Saito, H. *et al*. DMDA-PatA mediates RNA sequence-selective translation
649 repression by anchoring eIF4A and DDX3 to GNG motifs. *Nat. Commun.* **15**, 7418
650 (2024).

651 42. Heuser, A. *et al*. Challenges for the Discovery of Non-Covalent WRN Helicase
652 Inhibitors. *ChemMedChem* **19**, e202300613 (2024).

653 43. Selvaratnam, L., Willson, T. M. & Schapira, M. Structural Chemistry of Helicase
654 Inhibition. *J. Med. Chem.* **68**, 4022–4039 (2025).

655 44. Iwatani-Yoshihara, M. *et al.* Discovery of Allosteric Inhibitors Targeting the
656 Spliceosomal RNA Helicase Brr2. *J. Med. Chem.* **60**, 5759–5771 (2017).

657 45. Saalau-Bethell, S. M. *et al.* Discovery of an allosteric mechanism for the
658 regulation of HCV NS3 protein function. *Nat. Chem. Biol.* **8**, 920–925 (2012).

659 46. Ferretti, S. *et al.* Discovery of WRN inhibitor HRO761 with synthetic lethality in
660 MSI cancers. *Nature* (2024) doi:10.1038/s41586-024-07350-y.

661 47. Omura, S. N. & Nureki, O. Chapter Two - General and robust sample
662 preparation strategies for cryo-EM studies of CRISPR-Cas9 and Cas12 enzymes. in
663 *Methods in Enzymology* (eds. Ke, A. & Tang, W.) vol. 712 23–39 (Academic Press,
664 2025).

665 48. Punjani, A., Rubinstein, J. L., Fleet, D. J. & Brubaker, M. A. cryoSPARC:
666 algorithms for rapid unsupervised cryo-EM structure determination. *Nat. Methods* **14**,
667 290–296 (2017).

668 49. Bepler, T. *et al.* Positive-unlabeled convolutional neural networks for particle
669 picking in cryo-electron micrographs. *Nat. Methods* **16**, 1153–1160 (2019).

670 50. Mirdita, M. *et al.* ColabFold: making protein folding accessible to all. *Nat.*
671 *Methods* **19**, 679–682 (2022).

672 51. Jumper, J. *et al.* Highly accurate protein structure prediction with AlphaFold.
673 *Nature* **596**, 583–589 (2021).

674 52. Emsley, P., Lohkamp, B., Scott, W. G. & Cowtan, K. Features and development
675 of *Coot*. *Acta Crystallogr. D Biol. Crystallogr.* **66**, 486–501 (2010).

676 53. Borbulevych, O. Y., Plumley, J. A., Martin, R. I., Merz, K. M. & Westerhoff, L. M.
677 Accurate macromolecular crystallographic refinement: incorporation of the linear
678 scaling, semiempirical quantum-mechanics program *DivCon* into the *PHENIX*
679 refinement package. *Acta Crystallogr. D Biol. Crystallogr.* **70**, 1233–1247 (2014).

680 54. Pettersen, E. F. *et al.* UCSF ChimeraX : Structure visualization for researchers,
681 educators, and developers. *Protein Sci.* **30**, 70–82 (2021).

682 55. Kiianitsa, K., Solinger, J. A. & Heyer, W.-D. NADH-coupled microplate
683 photometric assay for kinetic studies of ATP-hydrolyzing enzymes with low and high
684 specific activities. *Anal. Biochem.* **321**, 266–271 (2003).

685 56. Reytor Gonzalez, M. L. & Alonso del Rivero Antigua, M. Reviewing the
686 experimental and mathematical factors involved in tight binding inhibitors Ki values
687 determination: The bi-functional protease inhibitor SmCI as a test model. *Biochimie*
688 **181**, 86–95 (2021).

689 57. Comparative Protein Structure Modeling of Genes and Genomes | Annual
690 Reviews.
691 https://www.annualreviews.org/content/journals/10.1146/annurev.biophys.29.1.291.

692 58. Pearlman, D. A. *et al.* AMBER, a package of computer programs for applying
693 molecular mechanics, normal mode analysis, molecular dynamics and free energy
694 calculations to simulate the structural and energetic properties of molecules.
695 *Comput. Phys. Commun.* **91**, 1–41 (1995).

696 59. Case, D. A. *et al.* Amber20. Unpublished
697 https://doi.org/10.13140/RG.2.2.25321.36969 (2020).

698 60. Hornak, V. *et al.* Comparison of multiple Amber force fields and development
699 of improved protein backbone parameters. *Proteins Struct. Funct. Bioinforma.* **65**,
700 712–725 (2006).

701 61. Ivani, I. *et al.* Parmbsc1: a refined force field for DNA simulations. *Nat.*
702 *Methods* **13**, 55–58 (2016).

703 62. Joung, I. S. & Cheatham, T. E. Determination of Alkali and Halide Monovalent
704 Ion Parameters for Use in Explicitly Solvated Biomolecular Simulations. *J. Phys.*
705 *Chem. B* **112**, 9020–9041 (2008).

706 63. Wang, J., Wang, W., Kollman, P. A. & Case, D. A. Automatic atom type and bond
707 type perception in molecular mechanical calculations. *J. Mol. Graph. Model.* **25**, 247–
708 260 (2006).

709 64. Wang, J., Wolf, R. M., Caldwell, J. W., Kollman, P. A. & Case, D. A. Development
710 and testing of a general amber force field. *J. Comput. Chem.* **25**, 1157–1174 (2004).

711 65. Frisch, M. J. *et al.* Gaussian 03 Rev. E.01. (2016).

66. Bayly, C. I., Cieplak, P., Cornell, W. & Kollman, P. A. A well-behaved electrostatic potential based method using charge restraints for deriving atomic charges: the RESP model. *J. Phys. Chem.* **97**, 10269–10280 (1993).

67. Peters, M. B. *et al.* Structural Survey of Zinc-Containing Proteins and Development of the Zinc AMBER Force Field (ZAFF). *J. Chem. Theory Comput.* **6**, 2935–2947 (2010).

68. Jorgensen, W. L., Chandrasekhar, J., Madura, J. D., Impey, R. W. & Klein, M. L. Comparison of simple potential functions for simulating liquid water. *J. Chem. Phys.* **79**, 926–935 (1983).

69. Essmann, U. *et al.* A smooth particle mesh Ewald method. *J. Chem. Phys.* **103**, 8577–8593 (1995).

70. Ryckaert, J.-P., Ciccotti, G. & Berendsen, H. J. C. Numerical integration of the cartesian equations of motion of a system with constraints: molecular dynamics of n-alkanes. *J. Comput. Phys.* **23**, 327–341 (1977).

71. Van Gunsteren, W. F. & Berendsen, H. J. C. Algorithms for macromolecular dynamics and constraint dynamics. *Mol. Phys.* **34**, 1311–1327 (1977).

72. Humphrey, W., Dalke, A. & Schulten, K. VMD: Visual molecular dynamics. *J. Mol. Graph.* **14**, 33–38 (1996).

73. Fukuzawa, K., Watanabe, C., Okiyama, Y. & Nakano, T. How to Perform FMO Calculation in Drug Discovery. in *Recent Advances of the Fragment Molecular Orbital Method* (eds. Mochizuki, Y., Tanaka, S. & Fukuzawa, K.) 93–125 (Springer Singapore, Singapore, 2021). doi:10.1007/978-981-15-9235-5_7.

74. Mochizuki, Y. *et al.* A parallelized integral-direct second-order M?ller?Plesset perturbation theory method with a fragment molecular orbital scheme. *Theor. Chem. Acc.* **112**, 442–452 (2004).

75. Mochizuki, Y., Koikegami, S., Nakano, T., Amari, S. & Kitaura, K. Large scale MP2 calculations with fragment molecular orbital scheme. *Chem. Phys. Lett.* **396**, 473–479 (2004).

76. Mochizuki, Y. *et al.* The ABINIT-MP Program. in *Recent Advances of the Fragment Molecular Orbital Method* (eds. Mochizuki, Y., Tanaka, S. & Fukuzawa, K.) 53–67 (Springer Singapore, Singapore, 2021). doi:10.1007/978-981-15-9235-5_4.

77. Takaya, D. *et al.* FMODB: The World's First Database of Quantum Mechanical Calculations for Biomacromolecules Based on the Fragment Molecular Orbital Method. *J. Chem. Inf. Model.* **61**, 777–794 (2021).

Acknowledgements

We thank members of Nureki Laboratory for their support in cryo-EM data collection. MD calculations were performed using computational resources of the supercomputer system (HPE SGI8600) jointly operated by the Japan Atomic Energy Agency (JAEA) and the National Institutes for Quantum Science and Technology (QST). FMO calculations were performed as part of the activities of the FMO Drug Design Consortium (FMODD) using the supercomputer "Fugaku" at RIKEN (project ID: hp240162).

Funding

This work was supported by JSPS KAKENHI (grant number 25K02501), Sumitomo Foundation, Shionogi Infectious Disease Research Promotion Foundation, and Uehara Memorial Foundation to T.S. This research was also partially supported by Research Support Project for Life Science and Drug Discovery (Basis for Supporting Innovative Drug Discovery and Life Science Research (BINDS)) from Japan Agency for Medical Research and Development (AMED) under grant numbers JP25ama121012 (support No. 6021) to O.N., JP25ama121024 (support No. 5660) to H.K., and JP25ama121030 (Support No. 5726) to K.F.

764

765 **Author contributions**

766 K.S. purified proteins, collected the cryo-EM data, solved the structures, performed
767 biochemical experiments, analyzed data, and wrote the paper. H.I. and H.K. performed MD
768 simulations and wrote the paper. T.M. and K.F. performed FMO analysis and wrote the
769 paper. S.K. purified proteins and performed biochemical experiments. Y.K., K.H., and O.N.
770 assisted with cryo-EM data collection. C.O. and A.O. purified proteins. T.S. designed the
771 project, solved the structures, analyzed data, and wrote the paper.

772

773 **Corresponding author**

774 Correspondence and requests for materials should be addressed to T.S.

775

776 **Competing interests**

777 The authors declare no competing interests.

778

779 **Legends for Supplementary Videos**

780 **Supplementary Video 1** Overall structure of the AMNV-bound complex.

781 **Supplementary Video 2** AMNV binding site.

782 **Supplementary Table 1** Cryo-EM data collection statistics
783

	AMNV complex	PTV complex
Magnification	105,000	105,000
Voltage (kV)	300	300
Electron exposure (e^{-}/Å^{2})	49.8	50.2
Defocus range (μm)	−0.6 to −1.6	−0.6 to −1.6
Pixel size (Å)	0.83	0.83
No. of micrographs	12,466	8,102

784

785

Supplementary Table 2. Data processing and refinement statistics

	AMNV 3DFlex	AMNV HM	AMNV PM	PTV 3DFlex	PTV HM	PTV PM
Data processing						
EMDB ID	EMD-64478	EMD-64479	EMD-64480	EMD-64481	EMD-64482	EMD-64483
Symmetry imposed	C_1	C_1	C_1	C_1	C_1	C_1
Particle number	467,000	467,989	467,989	99,000	99,345	99,345
Map resolution*	3.14	2.88	2.91	3.32	3.12	3.08
Refinement						
PDB ID	9UT1	9UT3	9UT4	9UT5	9UT6	9UT7
Non-hydrogen atoms	18,986	10379	8607	18677	9514	8607
Protein residues	2436	1298	1138	2399	1195	1138
DNA residues	7	7	0	6	6	0
Zinc ion	1	1	0	1	1	0
Ligand	1	1	0	1	1	0
Model vs data CC (mask)	0.81	0.86	0.87	0.79	0.82	0.83
Mean B factor (Å^2)						
Protein	174.30	142.89	116.16	155.90	130.94	117.81
DNA	118.93	84.91		109.13	98.6	
RMS deviations						
Bond length (Å)	0.003	0.003	0.003	0.002	0.003	0.002
Bond angles (°)	0.762	0.533	0.616	0.657	0.554	0.574
Validation						
MolProbity score	1.69	1.59	1.25	1.66	1.88	1.62
Clash score	6.96	7.79	4.76	5.78	9.51	8.53
Ramachandran plot						
Favored (%)	97.89	98.52	98.85	98.06	98.56	98.41
Allowed (%)	2.11	1.48	1.15	1.94	1.44	1.59
Disallowed (%)	0	0	0	0	0	0

*FSC threshold of 0.143 was used.

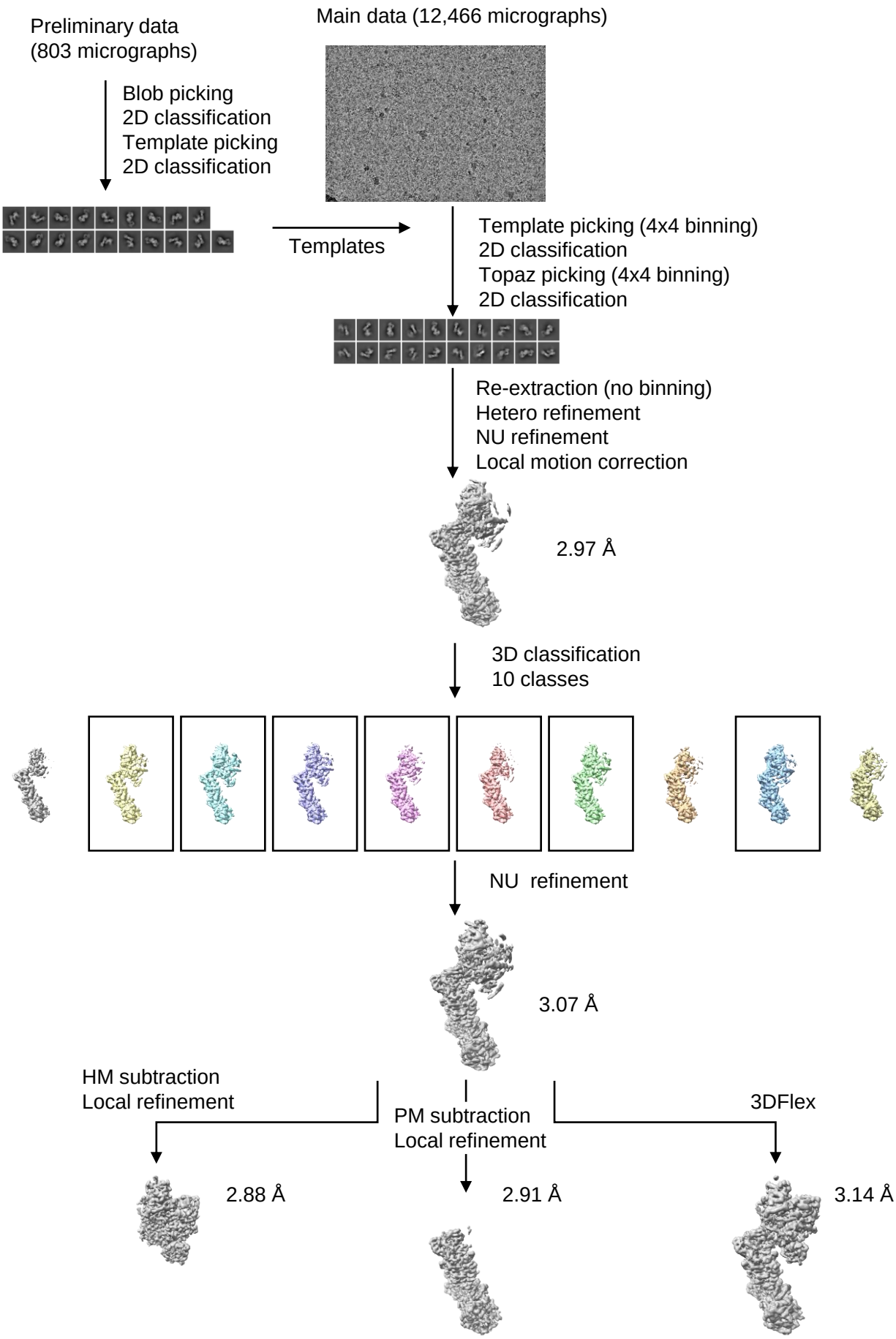

Extended Data Figure 1: Cryo-EM data processing of the AMNV complex.

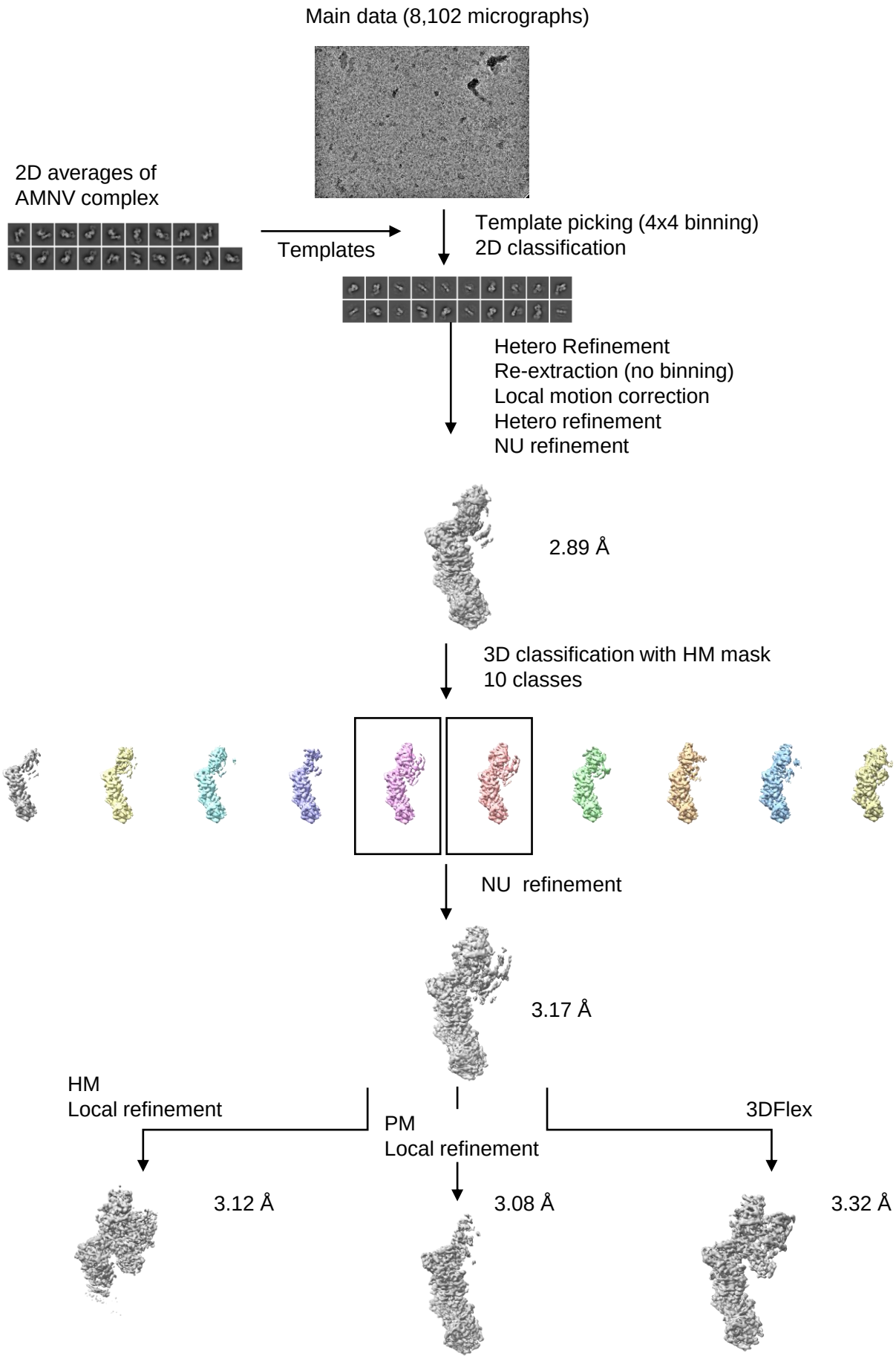

Extended Data Figure 2: Cryo-EM data processing of the PTV complex.

AMNV 3DFlex

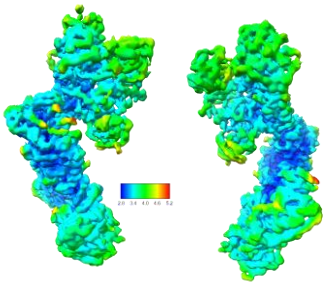

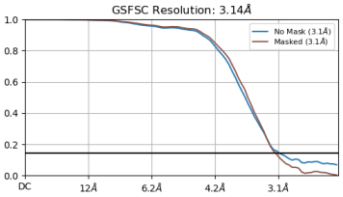

AMNV HM

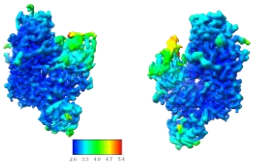

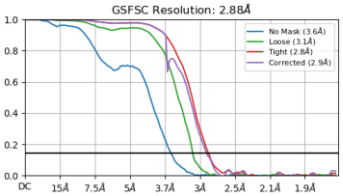

AMNV PM

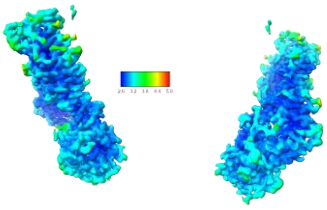

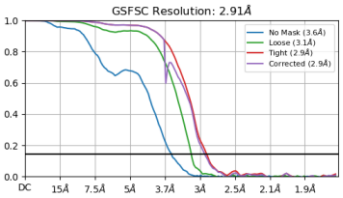

PTV 3DFlex

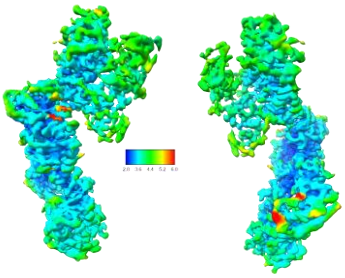

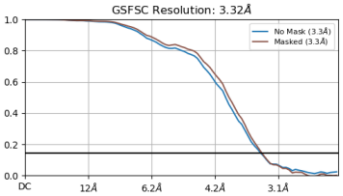

PTV HM

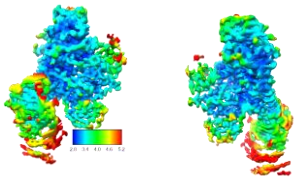

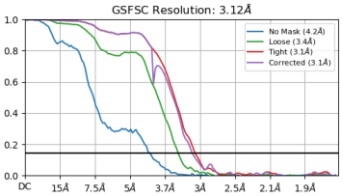

PTV PM

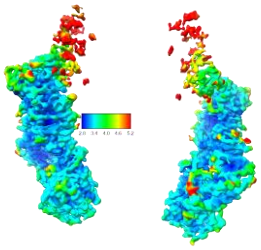

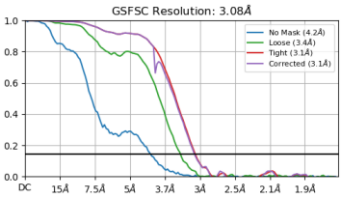

Extended Data Figure 3: Cryo-EM maps and resolutions of the AMNV and PTV complexes.

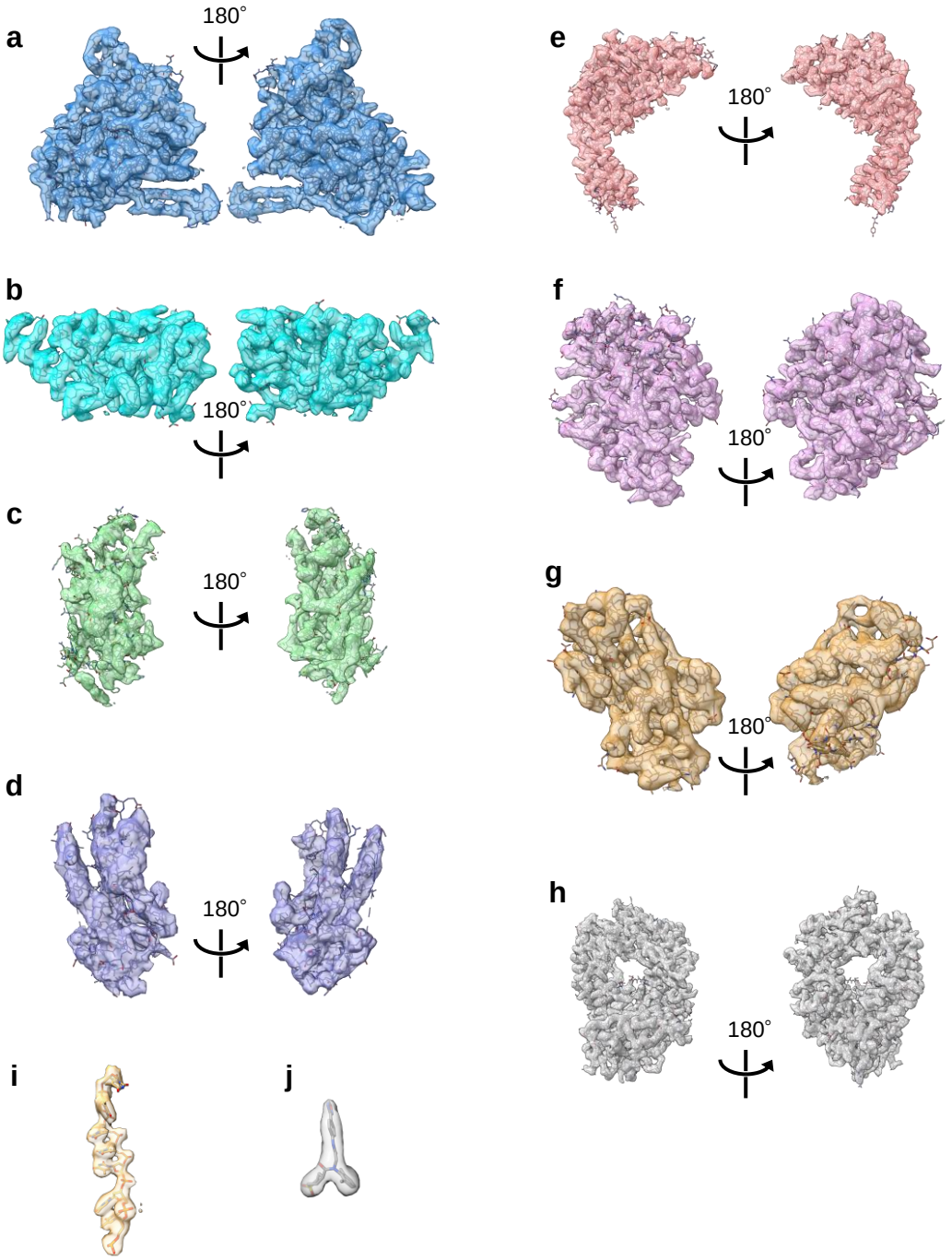

Extended Data Figure 4: Locally refined maps of individual domains of the AMNV complex. a, 1A. **b**, 2A. **c**, 2B. **d**, 2C. **e**, SD. **f**, PD. **g**, ZBD. **h**, UL8. **i**, ssDNA. **j**, ANMV.

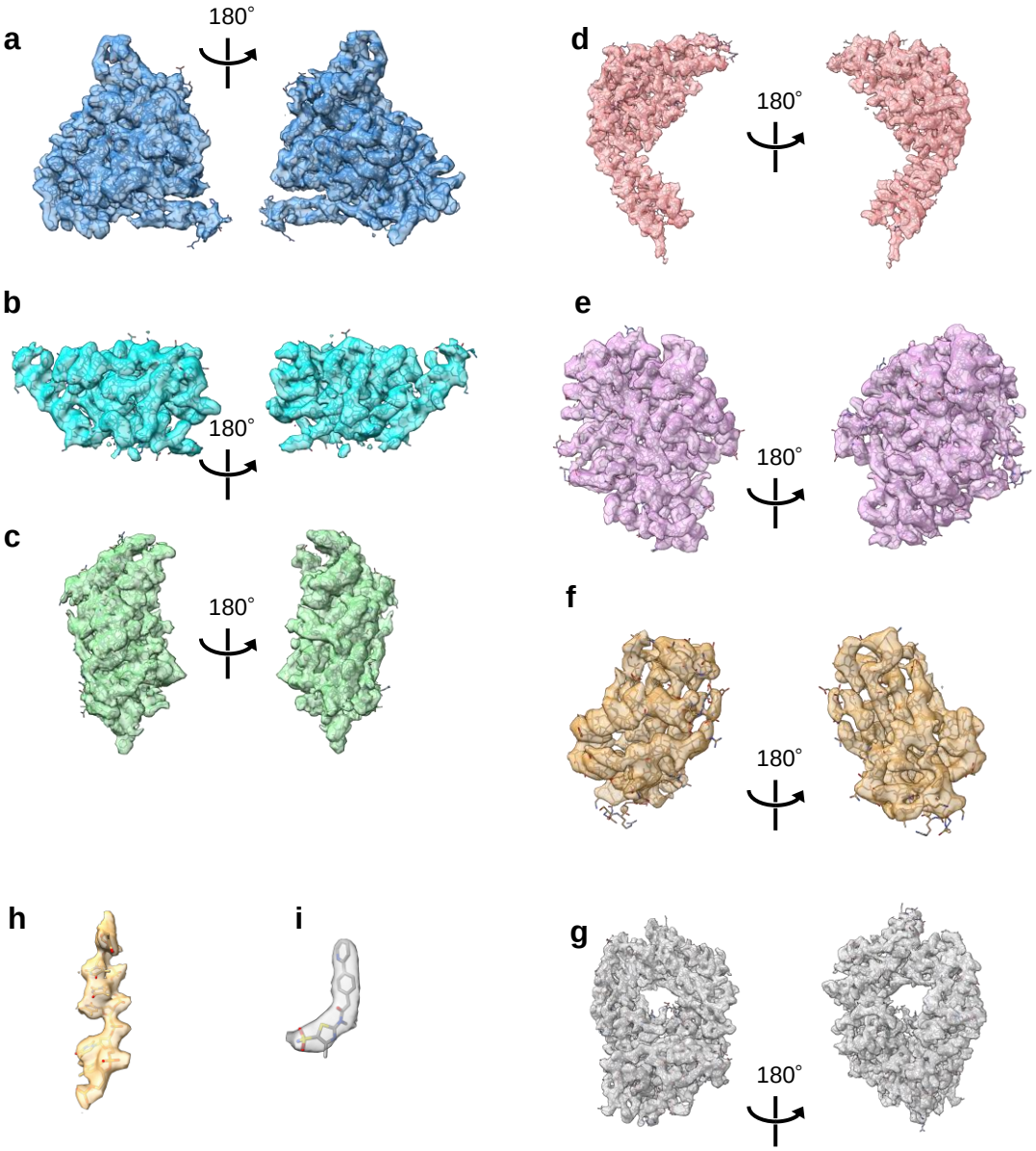

Extended Data Figure 5: Locally refined maps of individual domains of the PTV complex. No model was built for the domain 2C on the locally refined map of the helicase module of the PTV complex because of poor resolution. **a**, 1A. **b**, 2A. **c**, 2B. **d**, SD. **e**, PD. **f**, ZBD. **g**, UL8. **h**, ssDNA. **i**, PTV.

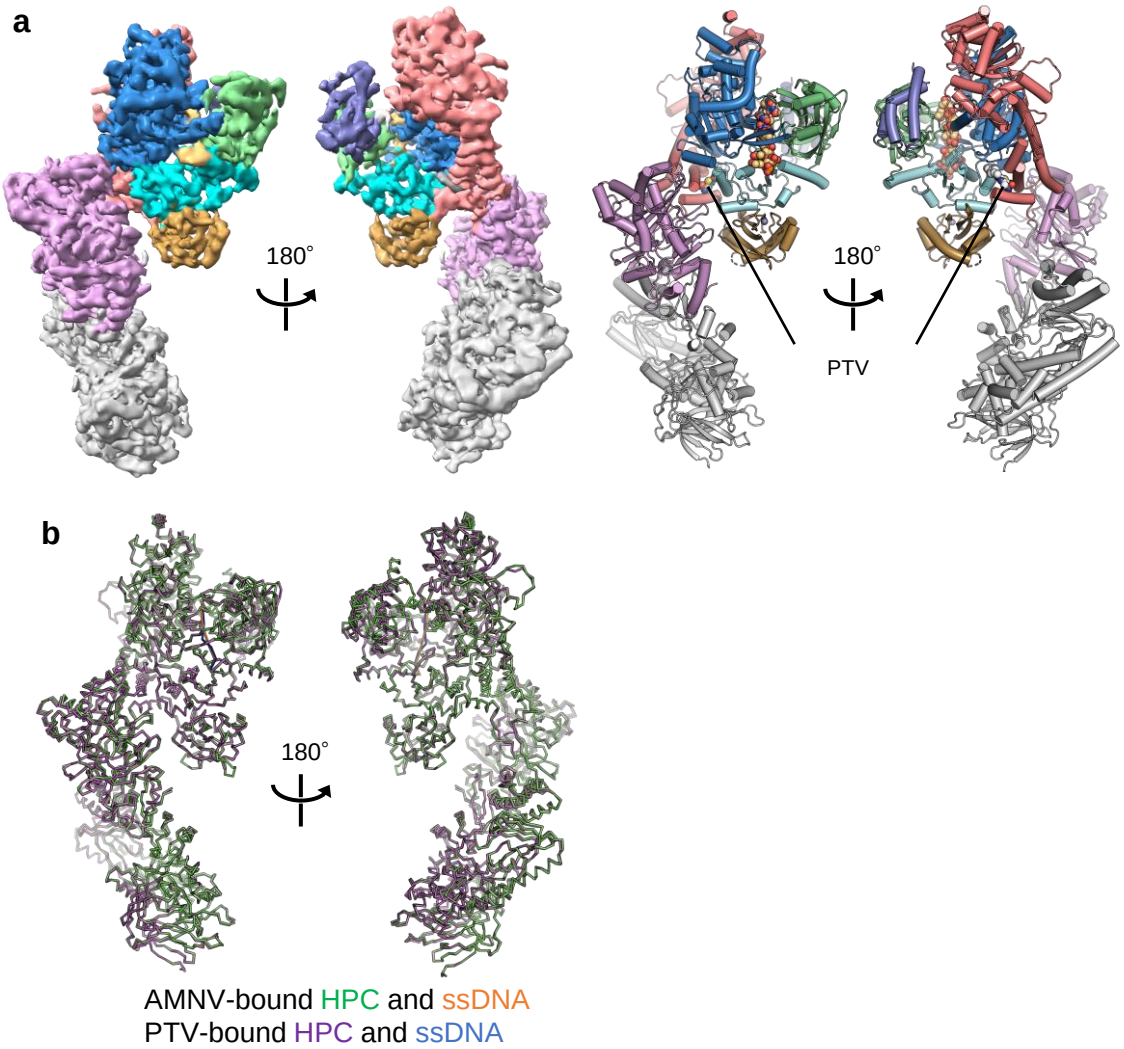

Extended Data Figure 6: Structure of the PTV-bound HPC. a, 3DFlex map (calculated using 3DFlex) and the ribbon model. **b**, Structural superposition of the AMNV- and PTV-bound complexes.

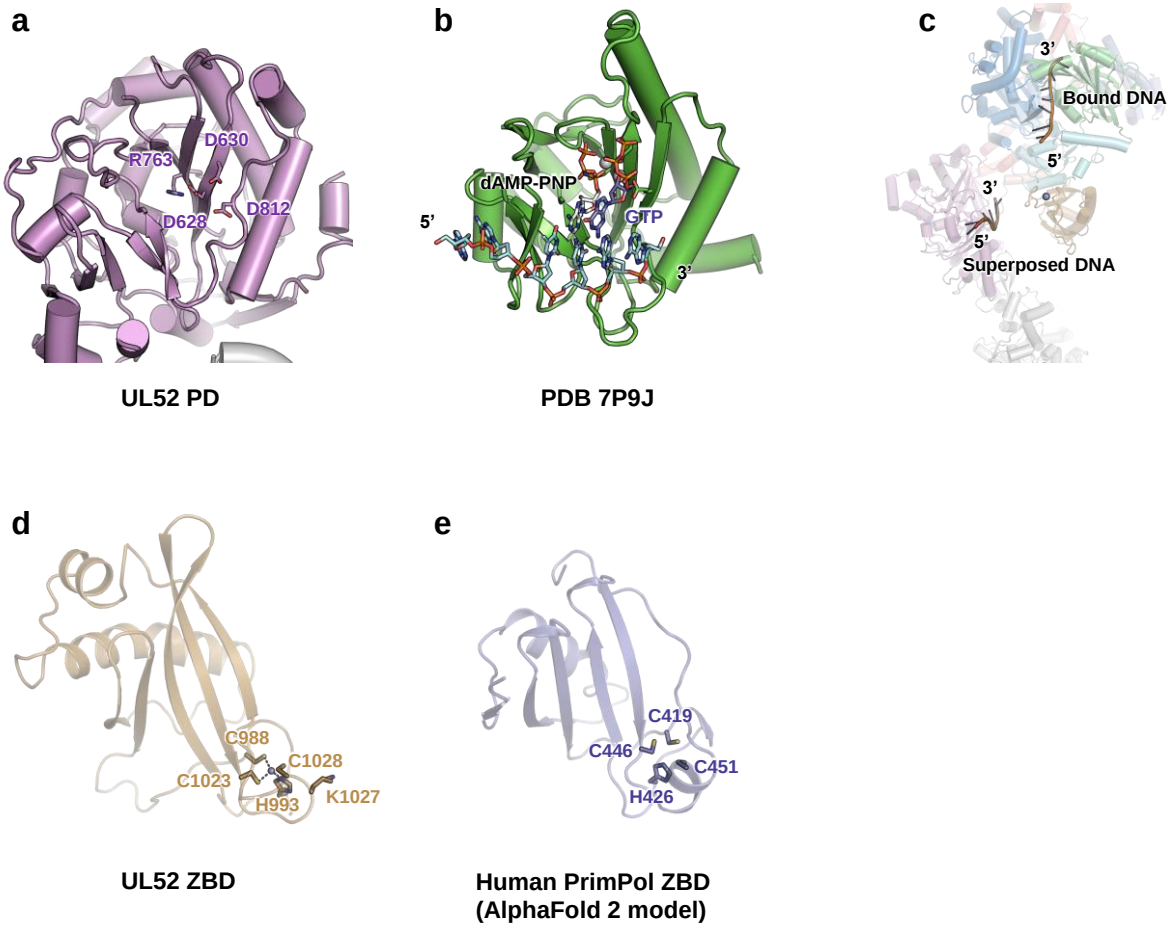

Extended Data Figure 7: Structures of the PD and ZBD. a, Structure of the PD. Key catalytic residues conserved among archaeo-eukaryotic primases are shown. **b**, Structure of the primer initiation complex of Prim-Pol domain of CRISPR-associated Prim-Pol (PDB 7P9J). The bound template DNA and two nucleotides (GTP and dAMP-PNP at the initiating and elongating sites, respectively) are also shown. **c**, Superposition of the structures of the AMNV-bound HPC and the template-bound Prime-Pol (only template DNA is shown). **d**, Structure of the ZBD of UL52 in the AMNV-bound HPC. Four zinc-coordinating residues as well as K1027, whose substitution abolishes the activities of HPC, are shown. **e**, A predicted structure of the ZBD (residues 366-468) of human PrimPol (UniProt Q96LW4), downloaded from AlphaFold Protein Structure Database. Possible zinc-coordinating residues are shown.

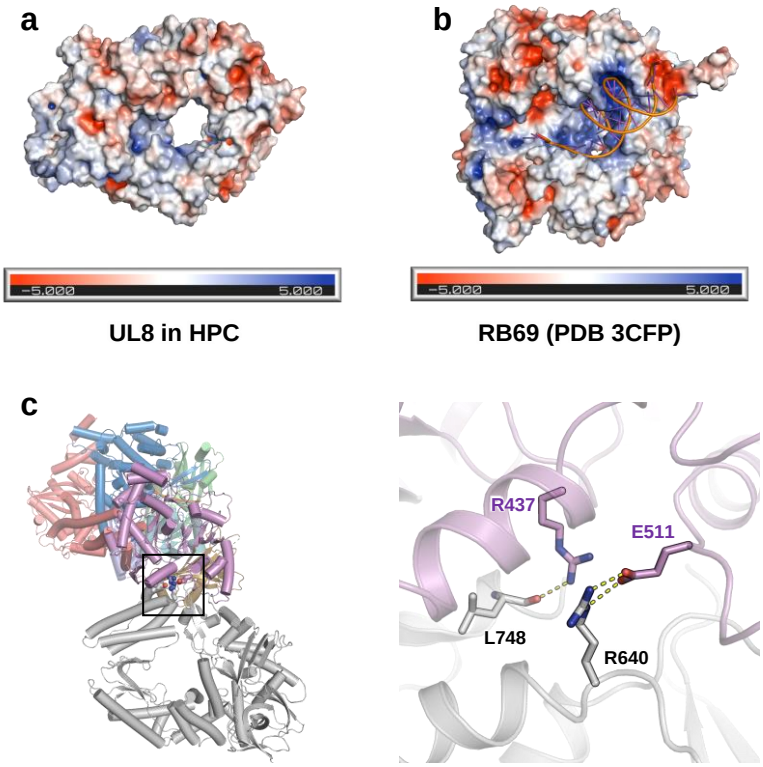

Extended Data Figure 8: Structure of UL8. a and **b**, Electrostatic surface potentials of UL8 (**a**) and RB69 (**b**), an α family DNA polymerase, bound with a DNA duplex. **c**, The UL52-UL8 interface. Left, the overall structure of HPC with the UL52-UL8 interface highlighted by a box. Right, A close-up view of the boxed region.

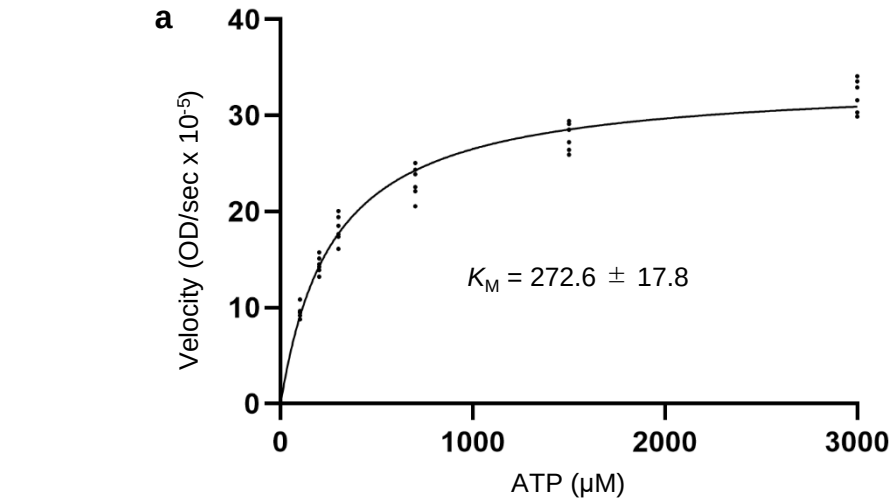

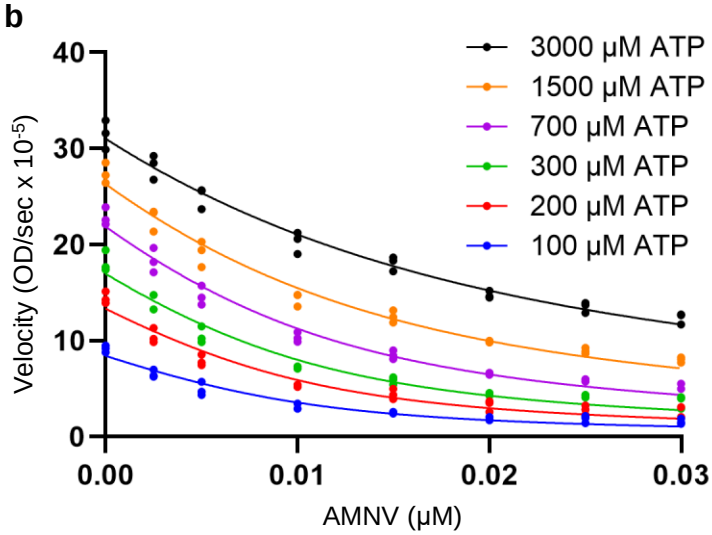

d

ATP (μM)	K_i^{app} (nM)
100	3.10 ± 0.46
200	3.52 ± 0.45
300	4.22 ± 0.48
700	5.47 ± 0.43
1500	8.41 ± 0.58
3000	14.34 ± 0.78

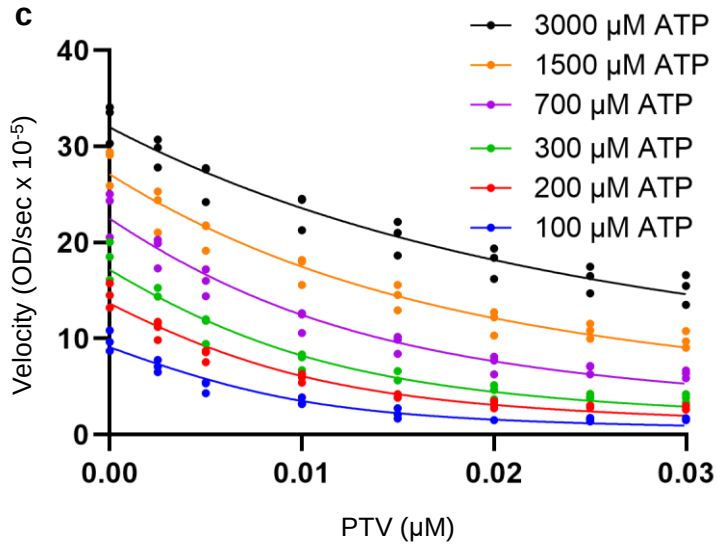

e

ATP (μM)	K_i^{app} (nM)
100	2.42 ± 0.40
200	3.61 ± 0.43
300	4.42 ± 0.60
700	6.90 ± 0.70
1500	11.72 ± 1.05
3000	20.67 ± 1.79

Extended Data Figure 9: ATPase assays. ***a***, Michaelis-Menten plot used to determine the K_M value for ATP from six independent experiments. Standard error of the mean (SEM) is also shown. ***b*** and ***c***, Relationship between reaction velocity and the concentrations of AMNV (***b***) or PTV (***c***) at varying ATP concentrations. ***d*** and ***e***, K_i^{app} values of AMNV (***d***) and PTV € determined under different ATP concentrations. SEM is also shown.

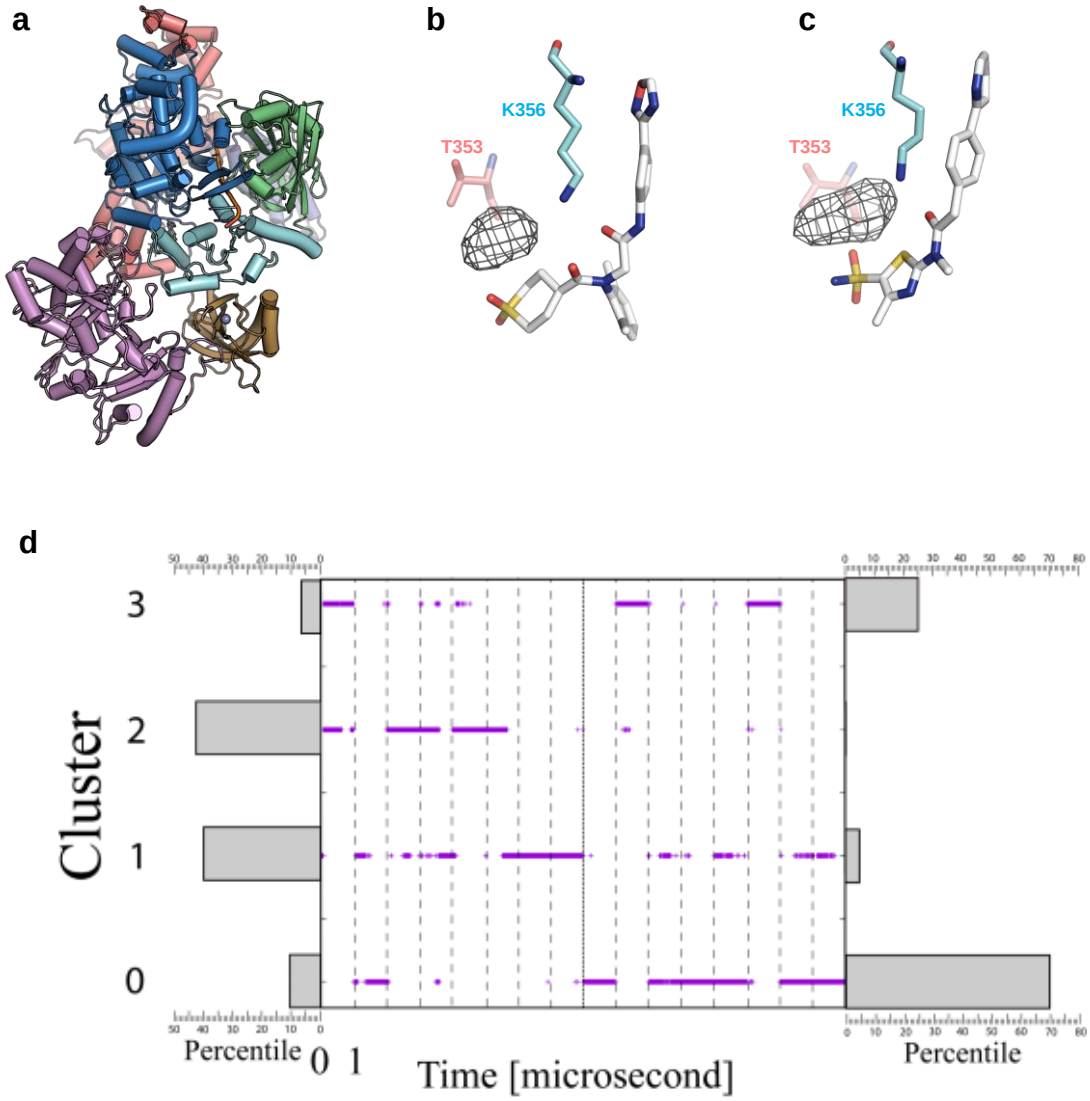

Extended Data Figure 10: MD analysis. a, The modeled structure of the UL5-UL52 subcomplex for MD simulations. b and c, The water density (shown as white mesh, contour level 0.3) within 4.5 Å from the oxygen atoms of the sulfonyl oxygen of AMNV (b) or the sulfonamide NH2 group of PTV (c) are shown. d. The existence percentiles and time distributions of the four clusters for the AMNV and PTV complexes during the MD trajectories are shown on the left and right, respectively. Existence percentiles are represented by bars, while temporal distributions are plotted over time. Vertical dashed lines indicate the one-microsecond MD simulation boundary for each replica (8 replicas per system).

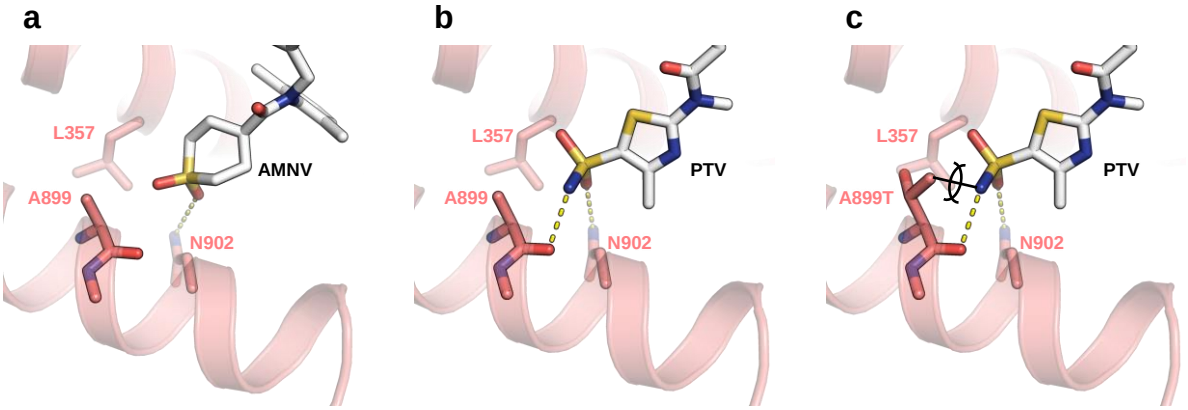

Extended Data Figure 11: A potential effect of UL52 A899 substitutions on PTV binding, but not AMNV. a, A hydrogen bond between the sulfonyl group of AMNV and the side chain of N902. **b**, Two hydrogen bonds between the sulfonamide group of PTV and both the side chain of N902 and the carbonyl group of A899. **c**, A structural model of the A899T substitution, which confers resistance to PTV. The Cγ atom of A899T is positioned too close to the amino group of PTV.

782 **Supplementary Table 1** Cryo-EM data collection statistics
783

	AMNV complex	PTV complex
Magnification	105,000	105,000
Voltage (kV)	300	300
Electron exposure (e^{-}/Å^{2})	49.8	50.2
Defocus range (μm)	−0.6 to −1.6	−0.6 to −1.6
Pixel size (Å)	0.83	0.83
No. of micrographs	12,466	8,102

784

785

Supplementary Table 2. Data processing and refinement statistics

	AMNV 3DFlex	AMNV HM	AMNV PM	PTV 3DFlex	PTV HM	PTV PM
Data processing						
EMDB ID	EMD-64478	EMD-64479	EMD-64480	EMD-64481	EMD-64482	EMD-64483
Symmetry imposed	C_1	C_1	C_1	C_1	C_1	C_1
Particle number	467,000	467,989	467,989	99,000	99,345	99,345
Map resolution*	3.14	2.88	2.91	3.32	3.12	3.08
Refinement						
PDB ID	9UT1	9UT3	9UT4	9UT5	9UT6	9UT7
Non-hydrogen atoms	18,986	10379	8607	18677	9514	8607
Protein residues	2436	1298	1138	2399	1195	1138
DNA residues	7	7	0	6	6	0
Zinc ion	1	1	0	1	1	0
Ligand	1	1	0	1	1	0
Model vs data CC (mask)	0.81	0.86	0.87	0.79	0.82	0.83
Mean B factor (Å^2)						
Protein	174.30	142.89	116.16	155.90	130.94	117.81
DNA	118.93	84.91		109.13	98.6	
RMS deviations						
Bond length (Å)	0.003	0.003	0.003	0.002	0.003	0.002
Bond angles (°)	0.762	0.533	0.616	0.657	0.554	0.574
Validation						
MolProbity score	1.69	1.59	1.25	1.66	1.88	1.62
Clash score	6.96	7.79	4.76	5.78	9.51	8.53
Ramachandran plot						
Favored (%)	97.89	98.52	98.85	98.06	98.56	98.41
Allowed (%)	2.11	1.48	1.15	1.94	1.44	1.59
Disallowed (%)	0	0	0	0	0	0

*FSC threshold of 0.143 was used.